Introduction

Astronomy is a science that is not short of superlatives, and this textbook is in keeping with this tradition as it investigates examples of **extreme environments** in the cosmos, such as any that are extremely hot, extremely energetic, extremely fast, have extremely strong gravitational fields, or all of these combined. There is an abundance of phenomena in the sky that deserve the label *extreme environment* — too many, in fact, to be dealt with in a single textbook. The specific selection presented here is strongly driven by the research interests of the authors, and we hope that our enthusiasm is still apparent even when arguments and derivations become more involved.

The underlying theme of the book is *accretion power* — the sometimes staggering amount of energy released when matter approaches gravitating bodies. This is particularly potent in the vicinity of compact objects — white dwarfs, neutron stars and black holes big and small — where the gravitational potential well is steep and deep. Accreting matter heats up enormously and emits powerful high-energy radiation.

This is why this textbook studies accreting systems with such compact objects. The main focus of the text is indeed on stellar mass accretors, i.e. compact binaries, where the accretion flows and their emission can be studied in great detail, revealing a wealth of exciting insights into matter and radiation under extreme conditions. Furthermore, we choose mainly to discuss disc accretion — in fact, the theory of accretion discs, and observational signatures of discs, make up a third of the book. As a result, the low-mass X-ray binaries receive relatively more attention than the brighter high-mass X-ray binaries. Wherever appropriate we present links to the much larger analogues of accretion-powered binaries, active galactic nuclei (AGN) that host supermassive black holes. Yet we place the emphasis firmly on the stellar systems, and do not present AGN in detail.

This book focuses on a discussion of the physical concepts underpinning our current understanding of accreting systems, and supports this by a presentation of key observational facts and techniques.

Our journey into the wild and wonderful world of high-energy astrophysics begins with a short review of the basics of mass accretion, of black holes, compact binaries and AGN, and the thermal emission that we expect from them. In Chapter 2 we consider the host systems of stellar mass accretors and study their evolutionary history and current evolutionary state. We then move on to develop a simple theoretical description for a flat, Keplerian disc in a steady state (Chapter 3). Chapter 4 presents the disc instability model for the spectacular outbursts seen in soft X-ray transients and dwarf novae. Chapter 5 focuses on observational properties, mainly in the optical waveband, that constitute proof of the existence of accretion discs, and touches upon some of the more advanced indirect imaging techniques of accretion flows. This leads to Chapter 6 (main author Robin Barnard) on the X-ray properties of accreting objects. In the past decade the X-ray observatories XMM-Newton and Chandra have opened up a new window into the world of stellar mass accreting systems in galaxies other than the Milky Way (the cover image of this book is meant to encapsulate this), and some of the systems discovered in other worlds are stranger than fiction. Chapter 7 (main author Hara Papathanassiou) examines the physics of very fast (relativistic) outflows and jets that are present in X-ray binaries, AGN and gamma-ray bursts, paving the way for Chapter 8 (main author Hara Papathanassiou), the culmination of the book, on the most energetic and most extreme events known in the Universe to date: gamma-ray bursts.

This book is designed to be a self-study text, and can be used as a resource for distance teaching courses. Moreover, even though it is pitched at the advanced undergraduate level, by the nature of the selected topics and the depth of presentation, an attempt is made to build on familiar concepts and develop them further, with a minimum of higher-level mathematics, showing derivations in more detail than similarly advanced texts do.

Part of this book draws on teaching texts of an earlier Open University course (*Active Galaxies* by Carole Haswell and *Interacting Binary Stars* by Ulrich Kolb), which in turn referred heavily to other sources. In particular, the influence of the advanced textbook *Accretion Power in Astrophysics* by Juhan Frank, Andrew King and Derek Raine is still apparent in this new book. Another treasure trove of inspiration and facts has been unpublished lecture notes by Hans Ritter.

Thanks go to Carolin Crawford for critical comments on an earlier manuscript of this book and to Philip Davis for checking the exercises and numerical examples.

Ulrich Kolb
Hara Papathanassiou
Robin Barnard

Chapter 1 Accretion power

Introduction

In this chapter we shall consider the concept of mass accretion in astrophysics and its importance as a source of energy. We shall identify accretion-fed compact objects as powerful energy generators, and review the astrophysical context where sustained accretion can occur. In preparation for a closer look at compact binary stars and active galactic nuclei (AGN), we develop the Roche model for close binaries, and review the evidence for the existence of supermassive black holes in AGN. We conclude the chapter with a simple analysis of the continuum emission expected from a plasma that accretes with angular momentum to form an accretion disc.

1.1 Accretion as a source of energy

One of the most important astrophysical processes in the Universe is **mass accretion**, where a gravitating body grows in mass by accumulating matter from an external reservoir. The key importance of this process, which we shall henceforth simply refer to as accretion, is that it liberates gravitational potential energy, making accreting objects potentially very powerful sources of energy.

The concept of a test mass

Throughout this book we shall often study the physical characteristics of accreting systems by considering the fate of a test mass. We define this to be a gravitating body with a very small mass, so much so that the effect of the test mass on any existing gravitational field, such as from gravitating bodies in its neighbourhood, is negligible. The geometric size of the test mass is also considered to be negligible, and hence the test mass is treated as a point mass in most cases.

1.1.1 Accretion luminosity

The essence of accretion is most easily illustrated by considering a test mass m in the gravitational field of a spherically symmetric body with mass M and radius R ($m \ll M$). The **gravitational potential energy** of the test mass at a distance r from the central body is

$$E_{\mathrm{GR}}(r) = -\frac{GMm}{r}. \tag{1.1}$$

As the test mass moves from a very large distance $r \to \infty$ to the surface $r = R$ of the central body, the energy difference $\Delta E_{\mathrm{GR}} = E_{\mathrm{GR}}(r = \infty) - E_{\mathrm{GR}}(R)$ is released. With $r \to \infty$ we have $1/r \to 0$ and so $E(r = \infty) \to 0$, hence

$$\Delta E_{\mathrm{GR}} = \frac{GMm}{R}. \tag{1.2}$$

Suppose now that the central body, the **accretor**, is accreting mass continuously at a rate $\dot{M}$. In the time interval Δt it will therefore accrete the mass $\Delta M = \dot{M} \times \Delta t$, and according to Equation 1.2 it will liberate the energy $\Delta E_{\rm GR} = GM\Delta M/R$. If *all* of this energy is radiated away at the same rate as it is liberated, the luminosity of the object due to the accretion process is $L_{\rm acc} = \Delta E_{\rm acc}/\Delta t$, which becomes

$$L_{\rm acc} = \frac{GM\dot{M}}{R}. \tag{1.3}$$

The quantity $L_{\rm acc}$ in Equation 1.3 is called the **accretion luminosity**.

Notation for time derivatives

Often the time derivative of a quantity is denoted by a dot over the symbol representing this quantity. As an example, the mass accretion rate is the rate at which mass is added to an object, i.e. the rate by which the mass M of this object increases. Therefore it can be written as

$$\frac{{\rm d}M}{{\rm d}t} \equiv \dot{M}.$$

It is instructive to estimate the actual mass accretion rate needed to achieve a significant accretion luminosity for a normal star like our Sun, and confront this value with mass flow rates observed in the Universe. Mass accretion rates are often expressed in solar masses per year, $\rm M_\odot\,yr^{-1}$. Equation 1.4 below provides the conversion into SI units.

Worked Example 1.1

Calculate the mass accretion rate needed to power an accretion luminosity of $1.0\,\rm L_\odot$ for the Sun.

Solution

We have

$$L_{\rm acc} = \frac{GM\dot{M}}{R} = 1\,\rm L_\odot$$

with $M = 1\,\rm M_\odot$ and $R = 1\,\rm R_\odot$. Solving this for the accretion rate, we obtain

$$\begin{aligned}\dot{M} &= 1\,\frac{\rm L_\odot R_\odot}{\rm GM_\odot}\\ &= \frac{3.83\times10^{26}\,\rm J\,s^{-1}\times6.96\times10^{8}\,m}{6.673\times10^{-11}\,\rm N\,m^2\,kg^{-2}\times1.99\times10^{30}\,kg}\\ &= 2.01\times10^{15}\,\rm kg\,s^{-1}.\end{aligned}$$

To convert this into $\rm M_\odot\,yr^{-1}$, we note that

$$\begin{aligned}1\,\rm M_\odot\,yr^{-1} &= \frac{1.99\times10^{30}\,\rm kg}{60\times60\times24\times365.25\,\rm s}\\ &= 6.31\times10^{22}\,\rm kg\,s^{-1}.\end{aligned} \tag{1.4}$$

Hence the required mass accretion rate for the Sun is

$$\dot{M} = \frac{2.01 \times 10^{15}}{6.31 \times 10^{22}}\,\mathrm{M_\odot\,yr^{-1}} = 3.2 \times 10^{-8}\,\mathrm{M_\odot\,yr^{-1}}.$$

To put this value into perspective, we note that the Sun is continuously shedding mass at the much smaller rate of about a few times $10^{-14}\,\mathrm{M_\odot\,yr^{-1}}$ in the form of the **solar wind**, a stream of high-energy particles emanating from the Sun's atmosphere. Even though massive stars and giant stars have much stronger stellar winds than the Sun, it would be difficult for a star like our Sun to accrete mass from the stellar wind of another star, at a rate similar to the one calculated here — not least as in any reasonable setting only a small fraction of the wind would be captured by the accreting star.

For a fixed mass accretion rate, the accretion luminosity obviously increases with the compactness M/R of the accreting object. This reflects the fact that for a given mass M, the depth of its gravitational potential well increases with decreasing radius R.

Exercise 1.1 The Sun would have to accrete mass at a rate of $3.2 \times 10^{-8}\,\mathrm{M_\odot\,yr^{-1}}$ to generate an accretion luminosity that rivals its own energy output powered by core-hydrogen burning.

(a) Calculate the accretion luminosity that a white dwarf with mass $1\,\mathrm{M_\odot}$ and radius $10^{-2}\,\mathrm{R_\odot}$ would have with the same accretion rate.

(b) Calculate the corresponding accretion luminosity for a neutron star with mass $1.4\,\mathrm{M_\odot}$ and radius $20\,\mathrm{km}$. ■

1.1.2 Accretion discs

Fluids and stellar plasma

Liquids and gases are collectively called **fluids**. In this book we are dealing with astrophysical fluids like stellar matter. Stellar matter is a gas, often referred to as stellar plasma or cosmic plasma. A **plasma** is a conducting fluid, e.g. an ionized gas, whose properties are determined by the existence of ions and electrons. Often stellar matter is fully ionized, but for low enough temperatures these ions and electrons may recombine to form neutral atoms and molecules.

Accreting matter hardly ever approaches the accretor in a straight-line trajectory. The conservation of angular momentum will in general lead to the formation of a flattened structure around the accretor in the plane perpendicular to the net angular momentum vector of the material. This plane could, for example, be the orbital plane of a binary system if the accreting material is donated from a companion star. Individual plasma blobs in such an **accretion disc** (Figure 1.1) orbit the accretor many times while maintaining a slow drift inwards, thereby losing angular momentum and gravitational potential energy. An accretion disc

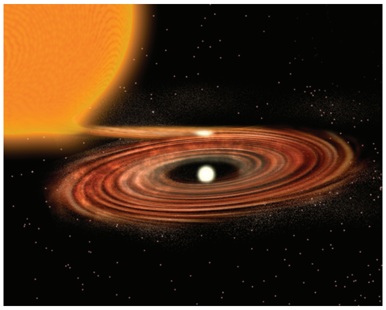

Figure 1.1 An artist's impression of an accretion disc.

acts as an agent to allow the accreting plasma to settle gently on the mass accretor. In fact, accretion discs are like machines that extract gravitational potential energy and angular momentum from plasma.

In most cases, plasma at a distance r from a spherically symmetric accretor with mass M will orbit the accretor on a circular orbit with speed

$$v_{\mathrm{K}} = \left(\frac{GM}{r}\right)^{1/2}. \tag{1.5}$$

The plasma is said to execute a **Kepler orbit** (or Keplerian orbit), and the speed v_{K} is the Kepler speed.

- How does Equation 1.5 follow from the statement that the centripetal force on a blob of plasma with mass m arises from the gravitational force?

- The gravitational force on a plasma blob with mass m is GMm/r^2, while the centripetal force is mv^2/r. Equating these, cancelling m, and rearranging for $v = v_{\mathrm{K}}$ reproduces Equation 1.5.

The orbit of a blob of plasma in an accretion disc is in fact a Kepler orbit with a slowly decreasing radius r. Hence the blob slowly drifts towards the accretor, losing gravitational potential energy while gaining kinetic energy.

The kinetic energy of a blob of plasma with mass m is

$$E_{\mathrm{K}} = \frac{1}{2}mv^2 = \frac{1}{2}\frac{GMm}{r},$$

while the gravitational potential energy is given by Equation 1.1. So we have

$$E_{\mathrm{K}} = -\tfrac{1}{2}E_{\mathrm{GR}}, \tag{1.6}$$

and the total energy of the system is

$$E_{\mathrm{tot}} = E_{\mathrm{K}} + E_{\mathrm{GR}} = \tfrac{1}{2}E_{\mathrm{GR}}. \tag{1.7}$$

The virial theorem

The **virial theorem** is a powerful diagnostic for a self-gravitating system in **hydrostatic equilibrium**, i.e. in a state where the system as a whole neither expands nor contracts as time goes by. The virial theorem relates the total gravitational potential energy E_{GR} of the system to its total kinetic energy E_{K} as

$$E_{\mathrm{K}} = -\tfrac{1}{2}E_{\mathrm{GR}}. \qquad \text{(Eqn 1.6)}$$

Equations 1.6 and 1.7 show that half of the released gravitational potential energy is converted into kinetic energy of the blob, while the other half is available to heat the plasma and to power the emission of electromagnetic radiation such as visible or ultraviolet light, or X-rays.

When calculating the accretion luminosity of disc accretion, it is therefore appropriate to include the factor $\frac{1}{2}$ in Equation 1.3 to take account of the fact that only half of the energy expressed by Equation 1.2 is available to be radiated away by the disc itself:

$$L_{\rm disc} = \frac{1}{2}\frac{GM\dot{M}}{R}. \tag{1.8}$$

1.1.3 Accretion efficiency

A useful measure that illustrates the power of accretion as an energy generator is the accretion efficiency $\eta_{\rm acc}$, defined by the expression

$$L_{\rm acc} = \eta_{\rm acc}\dot{M}c^2, \tag{1.9}$$

where c is the speed of light. In general, the efficiency η expresses the amount of energy gained from matter with mass m, in units of its mass energy, $E = mc^2$.

Exercise 1.2 Estimate the efficiency of accretion onto a neutron star. Compare Equations 1.9 and 1.3, and use typical parameters of a neutron star, such as $M = 1\,{\rm M}_\odot$ and $R = 10\,{\rm km}$.

Exercise 1.3 (a) Compare the efficiency (= energy gain/mass energy of input nuclei) of nuclear fusion of hydrogen into helium with the result of Exercise 1.2. The mass defect of hydrogen burning is $\Delta m = 4.40 \times 10^{-29}\,{\rm kg}$.

(b) Explain why accretion can be regarded as the most efficient energy source in the Universe. ■

The above exercises demonstrate that mass accretion has particularly significant consequences if it involves a compact accretor, i.e. an object with a higher density than that of normal stars or planets. Examples of stellar mass compact objects are stellar end-states such as white dwarfs or neutron stars, and the more exotic black holes. Both white dwarfs and neutron stars are subject to an upper mass limit. For white dwarfs this is the Chandrasekhar limit of $1.4\,{\rm M}_\odot$, while for neutron stars the limit is less securely known but is thought to be $\lesssim 3\,{\rm M}_\odot$. Black holes, on the other hand, apparently exist over a very wide range of masses. Stellar mass black holes are seen in binary systems, and supermassive black holes with masses up to $10^{11}\,{\rm M}_\odot$ in the nuclei of active galaxies.

Black holes are the most exotic of the accreting compact objects that we discuss here, so in the next section we shall review some basic facts about black holes that are relevant for accretion physics.

1.2 Black hole accretors

A black hole forms when self-gravity causes material to collapse to such high densities that the escape velocity reaches the speed of light.

1.2.1 Schwarzschild black holes

Using Newtonian dynamics we can calculate the magnitude of the escape velocity $v_{\rm esc}$ from the surface of a spherically symmetric gravitating body with mass M and radius R by saying that the kinetic energy of a mass m travelling vertically upwards with speed $v_{\rm esc}$ must equal the change in gravitational potential energy, as given by Equation 1.2, required to completely escape from the body's gravitational field, i.e.

$$\tfrac{1}{2}mv_{\rm esc}^2 = \frac{GMm}{R}.$$

Cancelling m and solving for $v_{\rm esc}$, we have

$$v_{\rm esc} = \left(\frac{2GM}{R}\right)^{1/2}. \tag{1.10}$$

To self-consistently calculate the magnitude of the escape velocity from an object with a density so high that the escape velocity reaches the speed of light, requires the use of general relativity. The relevant solution of Einstein's field equations is called the Schwarzschild solution, describing non-rotating black holes. These are therefore often referred to as **Schwarzschild black holes**. By a lucky coincidence, the correct general relativistic result for a non-rotating black hole is exactly what we obtain by setting $v_{\rm esc} = c$ in Equation 1.10. A non-rotating black hole is formed when a mass M collapses to within a sphere of radius $R_{\rm S}$, where

$$R_{\rm S} = \frac{2GM}{c^2} \tag{1.11}$$

is the **Schwarzschild radius**, the radius of the sphere surrounding the collapsed mass at which the escape speed equals the speed of light. Within this sphere is a region of spacetime that is cut off from the rest of the Universe, since neither light nor any other form of information can escape from it. The sphere itself is known as the **event horizon**. Immediately outside the event horizon is a region of spacetime in which there is an extremely strong gravitational field.

A black hole forms at the end of the life of a massive star when there is no pressure source sufficient to oppose the self-gravitational contraction of the remnant stellar core. Similarly, if a much larger mass collapsed under self-gravity, a black hole would ultimately form, and indeed it is now thought that black holes of mass $M \gtrsim 10^6\,{\rm M}_\odot$ are present at the cores of most (or possibly all) galaxies.

Accreting black holes offer the opportunity to study black hole properties since the energy generated through the accretion process makes these holes quite conspicuous. As we have discussed above, the accreting material will orbit the black hole before it crosses the Schwarzschild radius. In general relativity there is a **minimum stable circular orbit** close to the black hole, at about $3R_{\rm S}$. Closer to the black hole, a stable orbit does not exist, and material will plunge towards the event horizon so swiftly that any energy is effectively trapped in the plasma and hence disappears with the matter down the hole. The framework of general relativity is needed to work out the accretion luminosity and accretion efficiency of an accreting black hole; this is beyond the scope of this book. Instead, we apply here the Newtonian expressions to obtain estimates for these quantities, and just note the general relativistic result.

Exercise 1.4 Estimate the accretion efficiency onto a non-rotating black hole by assuming that the accreting material executes Kepler orbits in an accretion disc and slowly drifts inwards. Assume that the inner edge of the accretion disc coincides with the last stable circular orbit at $3R_{\rm S}$. ■

The correct general relativistic result for the accretion efficiency of a Schwarzschild black hole that accretes from a geometrically thin accretion disc is $\eta_{\text{acc}} = 5.7\%$.

1.2.2 Rotating black holes

Most stars acquire angular momentum when they form, and, unless there is an effective braking mechanism at work that removes spin angular momentum, will keep it throughout their evolution. So the black hole remnant of a star is expected to rotate, too. The Schwarzschild solution of Einstein's field equations for non-rotating black holes can be generalized in the form of the more involved Kerr solution to describe rotating black holes, or **Kerr black holes** (Figure 1.2).

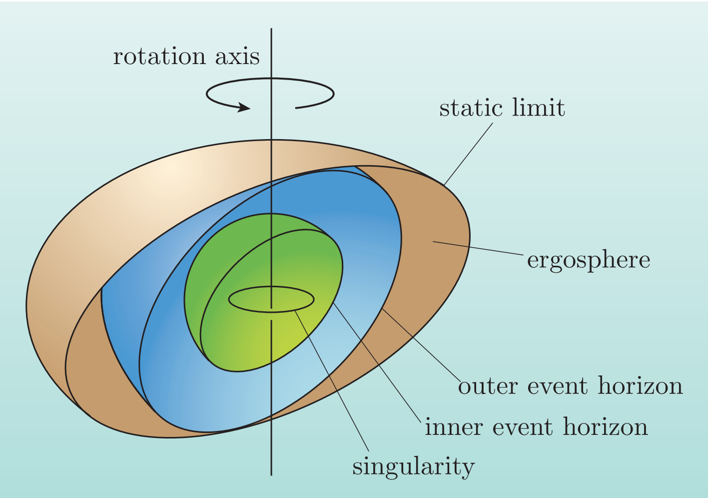

Figure 1.2 Critical surfaces of a Kerr black hole.

Both Schwarzschild and Kerr black holes represent gravitational singularities where the curvature of spacetime is infinite. In the case of Kerr black holes this singularity is a ring in the plane perpendicular to the rotational axis, while it is a single point for Schwarzschild black holes. Both types have a spherical event horizon where the escape speed is the speed of light. However, the (outer) event horizon of a Kerr black hole is surrounded by a second critical surface, the **static limit**, which has the shape of an oblate spheroid and touches the event horizon at its poles. The space between these two surfaces is called the **ergosphere**. Within the ergosphere the spacetime is dragged in the direction of the spinning black hole at a speed greater than c with respect to the outside Universe at rest, while at the static limit this speed equals c. As a consequence, matter inside the ergosphere cannot stay at rest. The material may even be ejected from the ergosphere by gaining energy from the black hole spin, thus spinning down the hole. If such a process could be sustained, the spinning black hole would eventually become a Schwarzschild black hole. There is also a maximum spin rate for a Kerr black hole.

In the context of accretion, a significant property of Kerr black holes is that the radius of the last stable orbit of matter orbiting the black hole outside of the event horizon decreases with increasing black hole spin (if the spin is in the same direction as the orbital motion of the accreting material). It is appropriate to use the last stable circular orbit in the expression for the accretion luminosity of a Kerr black hole.

- The last stable circular orbit for a Kerr black hole spinning at its maximum rate is $0.5R_\mathrm{S}$. Using the same Newtonian method as in Exercise 1.4, estimate the accretion efficiency.

- With

$$\eta_\mathrm{acc} = \frac{1}{2}\frac{GM}{Rc^2}$$

and $R = 0.5R_\mathrm{S}$, we obtain $\eta_\mathrm{acc} = 0.5 = 50\%$. The correct general relativistic result is $\eta_\mathrm{acc} = 0.32 = 32\%$.

1.3 Accreting systems

The accretion of mass is a very common phenomenon in the Universe. The Earth is constantly bombarded by meteorites and interplanetary dust particles (while also losing mass in the form of gas into space). Stars may sweep up interstellar matter as they cruise through clouds of hydrogen gas and dust. Such incidental, if not serendipitous, accretion rarely gives rise to appreciable accretion-powered emission. One notable exception is the high-energy emission from apparently isolated neutron stars that may accrete from the interstellar medium. For accretion to power sustained emission, a large enough mass reservoir must donate matter towards the accretor at a high enough rate.

This is the case, for example, in protoplanetary discs (proplyds). These circumstellar discs of dense gas surrounding newly formed stars (T Tauri stars) are the remnants of the star formation process and the birthplace of planetary systems.

Yet for accretion to power high-energy emission a compact accretor has to be present. There are principally two different groups of astrophysical systems with accreting compact objects, and throughout this book we shall look at each in more detail. The first group is compact binaries, systems with a compact star accreting matter from a companion, in most cases a normal star, either via the stellar wind of this star, or by a process called Roche-lobe overflow. The second group comprises supermassive black holes, with a mass in excess of $10^6\,\mathrm{M}_\odot$, in the centres of galaxies, that swallow clouds of interstellar gas and dust, or even whole stars, from their vicinity.

1.3.1 Interacting binary stars

A binary star is a system consisting of two stars that orbit the common centre of mass. Binaries are very common as the star formation process involves the collapse and fragmentation of interstellar clouds, favouring the formation of protostars in close proximity to each other. Newly formed triple systems and higher multiples are gravitationally unstable and will eventually reduce to binary stars (or hierarchical binary stars) and single stars through the ejection of component stars.

In very wide binaries, the two stellar components will evolve just as they would do as single stars. If, on the other hand, two stars orbit each other in close proximity, neither of them can get arbitrarily large without feeling the restrictive presence of the second star. If one star becomes too large, the gravitational pull on its outer layers from the second star will become bigger than the pull towards its own centre of mass. Then mass is lost from one star and transferred to the other star. (See the box on 'Binary stars' below.) This is called **mass transfer**, and it will obviously give rise to accretion. It will also have an impact on the physical character of the two stars. If the mass accretor is an evolved, old star, it might rejuvenate when it acquires unspoilt, hydrogen-rich material. Conversely, once the mass donor has lost a significant amount of material, it may look much older than a star of its current mass usually would.

Binary stars

The binary component losing mass to the other component is called the mass **donor**, while the component on the receiving end is called the mass **accretor**. Here we refer to the accretor as the primary star, or just the **primary**, while the mass donor is the secondary star, or simply the **secondary**. This is because in many (but not all!) cases the accretor is more massive than the donor. Quantities carrying the index '1' usually refer to the primary, while those with index '2' refer to the secondary. The **mass ratio**

$$q = \frac{\text{donor mass}}{\text{accretor mass}} = \frac{M_2}{M_1} \tag{1.12}$$

is therefore the ratio of donor mass to accretor mass, and usually (but not always) less than unity. Unfortunately this is not a generally accepted convention, and other books or journal papers may define the mass ratio the other way round (M_1/M_2).

Pseudo-forces in a rotating frame

We shall now consider the physical foundation of the mass transfer process in greater detail. This is most conveniently discussed in a frame of reference that co-rotates with the binary. This frame rotates about the rotational axis of the orbital motion, i.e. an axis perpendicular to the orbital plane and intersecting this plane at the binary's centre of mass, with the same angular speed ω as the binary,

$$\omega = \frac{2\pi}{P_{\text{orb}}}, \tag{1.13}$$

where P_{orb} is the orbital period. The co-rotating frame does *not* constitute an **inertial frame**. **Pseudo-forces** (sometimes called fictitious forces) appear as a result of the rotational motion. To see why, we recall Newton's laws of motion. Any acceleration of a body in an inertial frame results from the action of a force on this body. In contrast, in a rotating frame a body may accelerate relative to the observer simply because the observer himself or herself is fixed to the rotating frame, while the body is not. The force causing this acceleration does not exist in the inertial frame, hence is called a pseudo-force. Nonetheless, for an observer in the rotational frame it can be very real.

In particular, there are two pseudo-forces in a rotating frame: the centrifugal force and the Coriolis force.

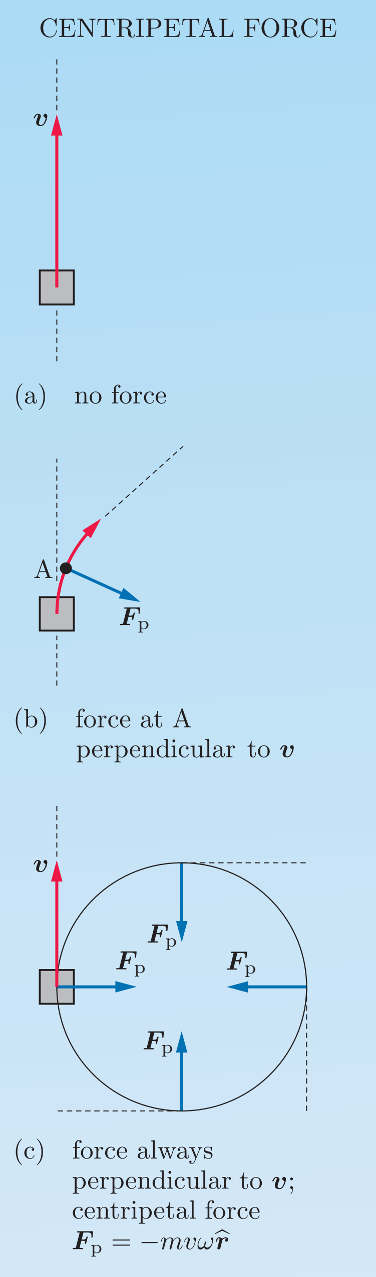

Figure 1.3 The centripetal force. The observer is in a non-rotating frame of reference (inertial frame).

The **centrifugal force** is a familiar pseudo-force that, for example, the driver of a car experiences when following a sharp bend of the road at high speed. The driver is an observer fixed to the rotating frame, the car. The rotational axis is vertical and passes through the geometric centre of the bend. The driver is at rest in the driver's seat, but to stay there, muscle strength is needed to balance the centrifugal force pushing the driver radially outwards, away from the centre of the bend. For an observer in the inertial frame at rest with respect to the road — someone standing on the pavement — the driver is of course not at rest, but travelling on a circular path. The pedestrian concludes that there is a **centripetal force** acting on the driver, which is pulling the driver off the straight line (Figure 1.3). This force is mediated by the friction of the tyres on the road, the structural rigidity of the car, and the driver's muscle strength. In fact, the centripetal force has the same magnitude as the centrifugal force, but the opposite direction. The magnitude of the centrifugal force on a body with mass m and distance r from the rotational axis is

$$F_c = m\frac{v^2}{r} = m\omega^2 r. \tag{1.14}$$

Here ω is the angular speed of the rotating frame, and $v = \omega \times r$ is the magnitude of the instantaneous velocity of a point fixed to the rotating frame, with respect to the non-rotating inertial frame.

The second pseudo-force in the rotating frame, the **Coriolis force**, acts *only* on bodies that are moving in this frame. The Coriolis force is always perpendicular to the direction of motion, and also perpendicular to the rotation axis. It is easy to see why such a force in addition to the centrifugal force must exist. A body at rest in an inertial frame would appear to move in a circle around the rotational axis in the rotating frame (Figure 1.4b). Hence the observer in the rotating frame concludes that there is a force at work that not only overcomes the outward centrifugal force, but also provides the inward centripetal force necessary to maintain the circular motion.

Worked Example 1.2

Use the example of a body at rest in the inertial frame to show that the Coriolis force has the magnitude $2m\omega v$. Consult Figure 1.4.

Solution

The body of mass m is at rest in the non-rotating frame. Its distance from the rotational axis is r. In the frame rotating with angular speed ω, the same body appears to move on a circle with radius r and speed $v = r\omega$.

The observer in the rotating frame concludes that there is a net force, the centripetal force $\boldsymbol{F}_p$, of magnitude $m\omega^2 r = m\omega v$ acting on the body. This force points towards the centre of the circle. The observer knows that there are two pseudo-forces acting on the body: the centrifugal force $\boldsymbol{F}_c$ of magnitude $m\omega^2 r = m\omega v$, pointing away from the centre, and the Coriolis force $\boldsymbol{F}_{\text{Coriolis}}$. From the vector sum

$$\boldsymbol{F}_{\text{net}} = \boldsymbol{F}_p = \boldsymbol{F}_c + \boldsymbol{F}_{\text{Coriolis}}$$

(see Figure 1.4b), we have

$$\boldsymbol{F}_{\text{Coriolis}} = \boldsymbol{F}_p - \boldsymbol{F}_c.$$

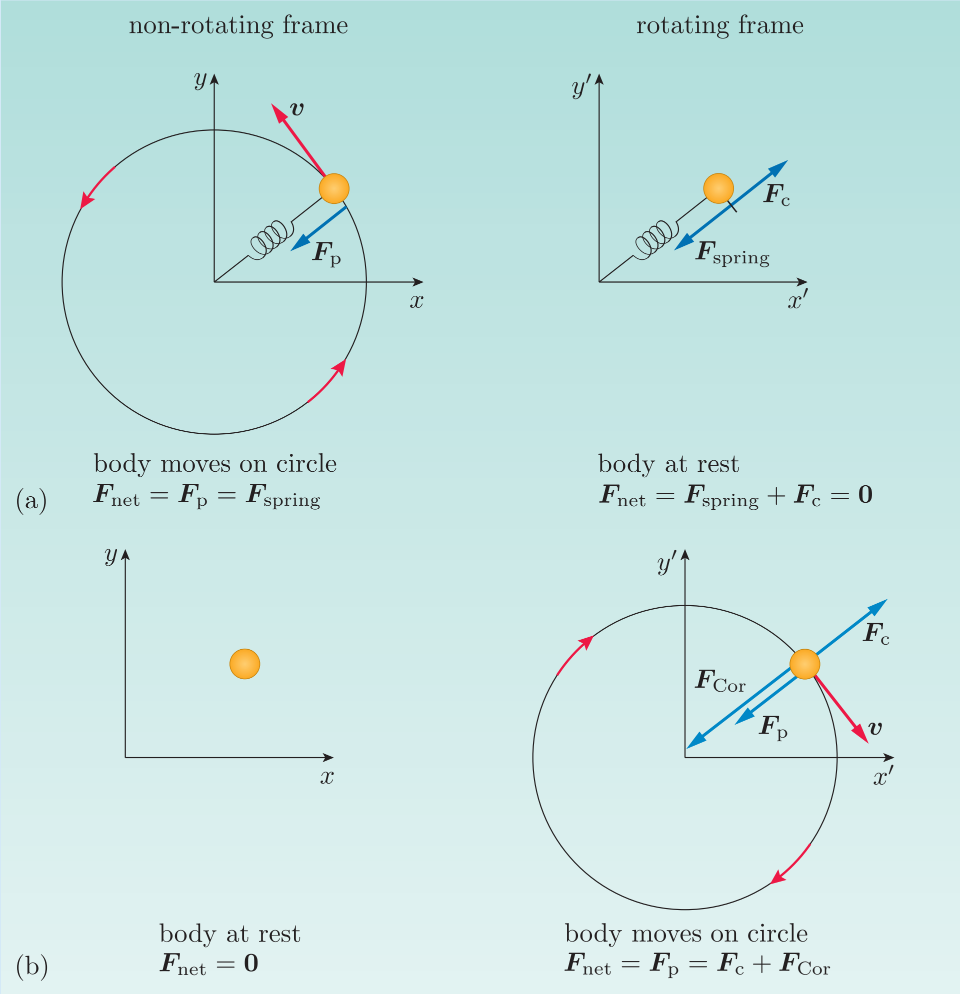

Figure 1.4 The Coriolis force. (a) A body is attached to a spring and moves on a circle with constant angular speed (as seen in the inertial frame). In the co-rotating frame the body is at rest; the net force on the body is zero — the spring force just balances the centrifugal force. (b) A body at rest in the inertial (non-rotating) frame is seen to move on a circle with constant angular speed in the rotating frame. The necessary centripetal force $\boldsymbol{F}_p$ for circular motion is given by the sum of the centrifugal force $\boldsymbol{F}_c$ and the Coriolis force $\boldsymbol{F}_{Coriolis}$.

As $\boldsymbol{F}_p$ and $\boldsymbol{F}_c$ point in opposite directions, it is clear that the magnitude of the Coriolis force is just the sum of the magnitudes of $\boldsymbol{F}_p$ and $\boldsymbol{F}_c$, i.e. $2m\omega v$, as required. (The expression for the Coriolis force is slightly more complicated if the velocity is not perpendicular to the rotation axis; it involves the vector product

$$\boldsymbol{F}_{Coriolis} = -2m\boldsymbol{\omega} \times \boldsymbol{v}, \tag{1.15}$$

so only the velocity component perpendicular to the axis is involved.)

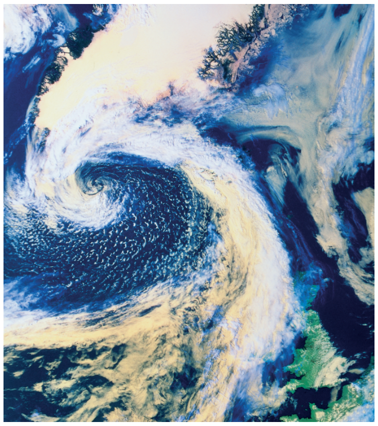

Figure 1.5 Earth as seen from space, with a cyclonic depression.

We do, in fact, live in a rotating frame of reference ourselves: on Earth. The Coriolis force is responsible for the motion of clouds around low-pressure weather systems, as seen in satellite images of the Earth (Figure 1.5). On the northern hemisphere, the Coriolis force deflects air moving towards a low-pressure region in a clockwise direction as seen from space. The air flow thus joins the anticlockwise, circular movement around the low-pressure area, a so-called cyclonic flow.

The magnitude and direction of the centrifugal force depends only on the position in the rotating frame. It can therefore be expressed as the gradient of a potential V, such that $\boldsymbol{F}_c \propto \boldsymbol{\nabla} V$. In contrast, the Coriolis force depends on position *and* velocity, and cannot be derived from a potential. In the context of the Roche model below, the most important thing to remember about the Coriolis force is that it vanishes if $v = 0$ in the rotating frame!

The Roche model

To arrive at a useful and yet simple quantitative description of a close binary system with mass exchange, we now make three simplifying assumptions. These will allow us to express the force $\boldsymbol{F}$ on a test mass m in the system in terms of the **Roche potential** Φ_R in the co-rotating frame as

$$\boldsymbol{F} = -m\boldsymbol{\nabla}\Phi_R.$$

- Express the physical meaning of this equation in words.

- The direction of the force on the test mass, as seen in the co-rotating frame, is in the opposite direction to the gradient of the potential. In the x-direction the gradient of Φ_R is just the derivative $d\Phi_R/dx$.

The first simplifying assumption is that the orbits of the binary components are circular. Close binaries with elliptical orbits do exist, but if one component has an extended envelope, then strong tidal forces within this envelope will act to reduce the eccentricity of the orbit on a short timescale. Most mass-transferring binaries do indeed have circular orbits.

The second assumption is that the two components are in effect point masses — which they clearly are not. However, the gas density inside stars increases markedly towards the centre. The bulk of the stellar mass is in fact concentrated in a small, massive core region that is practically unaffected by the presence of a companion, and hence the star can safely be approximated by a point mass.

The third assumption is that the outer layers of each of the stars rotate synchronously with the orbit. In close interacting binaries, tidal forces are indeed very effective in establishing the tidal locking of spin and orbit.

We consider now a test mass m fixed in the co-rotating frame (binary frame) at a position that we specify by the position vector $\boldsymbol{r}$ (see Figure 1.6). The primary with mass M_1 is at the position $\boldsymbol{r}_1$, the secondary with mass M_2 is at $\boldsymbol{r}_2$, and the centre of mass is at $\boldsymbol{r}_c$. The test mass is subject to the gravitational force of the primary, the gravitational force of the secondary, and the centrifugal force. The Coriolis force vanishes as the test mass is at rest in the binary frame.

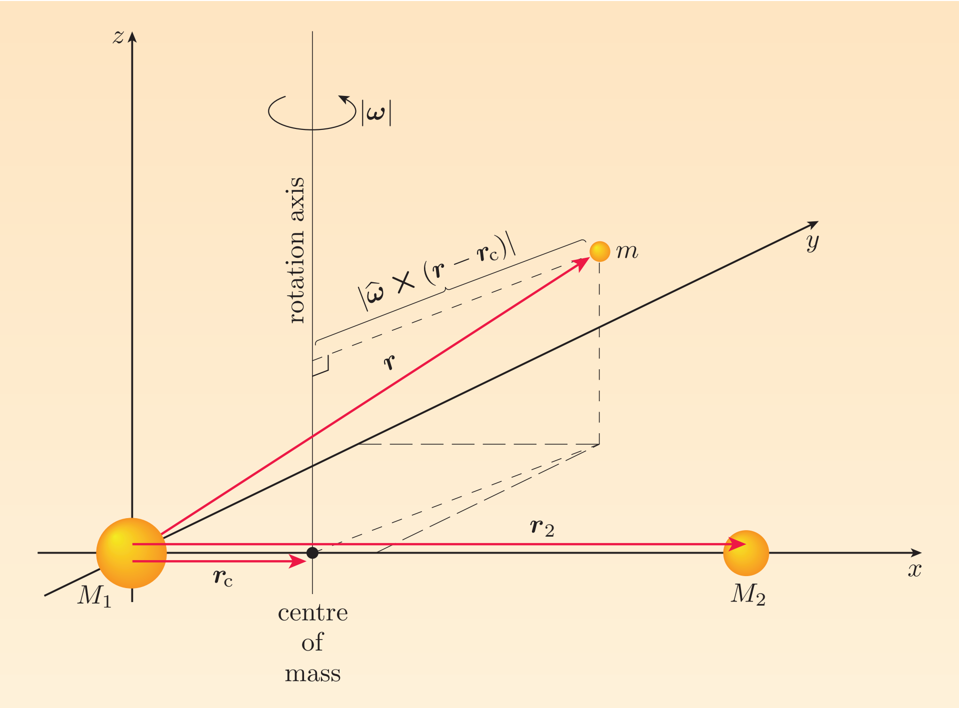

Figure 1.6 Definitions for the Roche model. The arrows representing $\boldsymbol{r}_\mathrm{c}$ and $\boldsymbol{r}_2$ are slightly displaced for clarity but they are coincident with the x-axis over the length of the vector in each case.

The Roche potential is then

$$\Phi_\mathrm{R}(\boldsymbol{r}) = -\frac{GM_1}{|\boldsymbol{r}-\boldsymbol{r}_1|} - \frac{GM_2}{|\boldsymbol{r}-\boldsymbol{r}_2|} - \tfrac{1}{2}\left(\boldsymbol{\omega}\times(\boldsymbol{r}-\boldsymbol{r}_\mathrm{c})\right)^2. \tag{1.16}$$

Exercise 1.5 In the expression 1.16 for the Roche potential $\Phi_\mathrm{R}(\boldsymbol{r})$, explain the functional form of the three terms on the right-hand side.

Exercise 1.6 Assume that the x-axis goes through the centres of the two stellar components, and the origin is at the centre of the primary. Write down the Roche potential as a function of x, and determine the direction and magnitude of the force on a test mass m at the centre of mass of the system. ■

The significance of the Roche potential is that in equilibrium, for negligible fluid flow velocities, the surfaces of constant Roche potential, the Roche equipotentials, are also surfaces of constant pressure. In particular, the *surface* of a star, i.e. the layer with an optical depth of about 1 (see the box entitled 'Cross-section, mean free path and optical depth' in Section 6.2 for a definition of optical depth), coincides with a Roche equipotential. Hence the shape of the Roche equipotential determines the *shape* of the stellar components in binary systems.

Figure 1.7 illustrates the shape of the Roche equipotentials. Close to the centre of one of the stars, say the secondary, the equipotentials are nearly spherical, somewhat flattened along the rotational axis — in the z-direction in the figure (panel (a) in Figure 1.7). As long as the stellar radius is small compared to the orbital separation, the star adopts the characteristic shape of a single star rotating with the orbital period of the binary. With increasing distance from the stellar

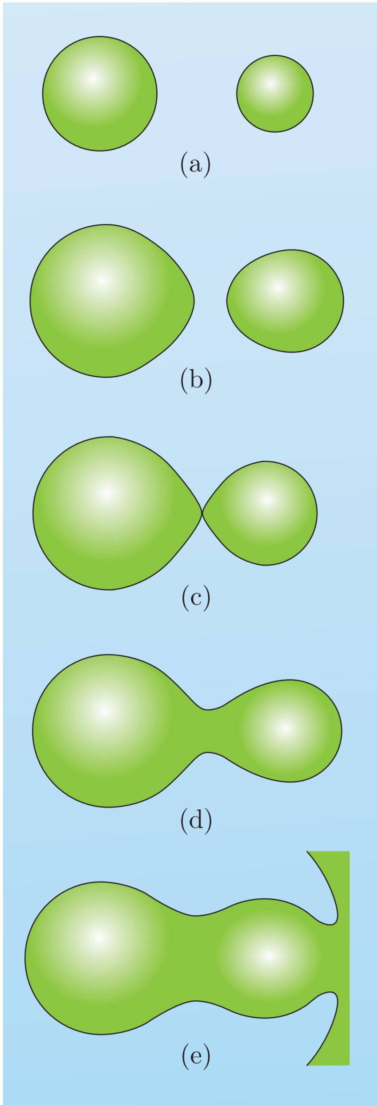

Figure 1.7 Roche equipotential surfaces for different values of Φ_R.

centre, the value of the Roche potential Φ_R increases (i.e. becomes less negative), and the corresponding equipotentials become more and more pointed towards the primary, while still excluding the primary's centre (panel (b) in Figure 1.7). The closed equipotential surface with the largest value of Φ_R (or smallest value of $|\Phi_\mathrm{R}|$) that still excludes the primary's centre touches the corresponding equipotential surface that encloses the primary's centre in one critical point, the L_1 point, or **inner Lagrangian point** (panel (c) in Figure 1.7). The L_1 point is a saddle point of the Roche potential.

Figure 1.8 A familiar surface with a saddle point.

- Describe the characteristics of a saddle point (see Figure 1.8).

- A saddle point of a potential is a point where the spatial gradient of the potential Φ vanishes, such that the potential is a maximum in one direction, e.g. along the x-axis, but a minimum in a direction perpendicular to the former, i.e. along the y-axis. Mathematically,

$$\frac{\partial \Phi}{\partial x} = \frac{\partial \Phi}{\partial y} = 0$$

and the second partial derivative $\partial^2\Phi/\partial x^2$ is negative, while $\partial^2\Phi/\partial y^2$ is positive. (See the box entitled 'Partial derivatives' in Subsection 3.2.2 for the meaning of the symbol ∂.)

The two lobes of the critical Roche equipotential surface that contains the L_1 point are the **Roche lobe** of the secondary and the Roche lobe of the primary star, respectively. Mass exchange between these stars will proceed through the immediate vicinity of the L_1 point. A stellar component of the binary can expand only until its surface coincides with this critical Roche equipotential. If such a **Roche-lobe filling** star attempts to expand further, mass will flow into the direction of decreasing values of Φ_R, i.e. into the lobe of the second star. This is called **Roche-lobe overflow**.

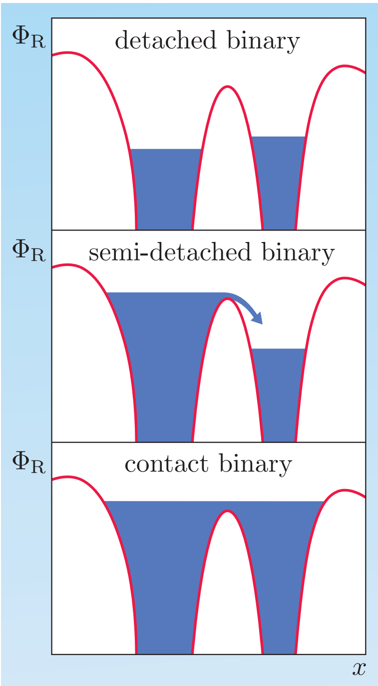

Figure 1.9 Schematic view of the potential wells of a detached, semi-detached and contact binary.

For somewhat larger values of Φ_R (smaller values of $|\Phi_\mathrm{R}|$), the equipotentials surround both stars, adopting a dumbbell-like shape (panel (d) in Figure 1.7), while at distances large compared with the orbital separation, the centrifugal component of the potential dominates, and near the orbital plane the equipotentials appear as nested cylinders aligned with the binary's orbital axis.

The values of the Roche potential along a line through the centres of the two binary star components provide an instructive illustration of Roche-lobe overflow (see Figure 1.9, where this line is the x-axis). The most notable features of the curve in this figure are the effect of the centrifugal repulsion at large distances from the binary's centre of mass (Φ_R falls off at large $|x|$), and the two deep valleys caused by the gravitational attraction of the corresponding star in the respective valley. A star can fill these valleys only up to the 'mountain pass' in between, the L_1 point. If the star attempts to grow further, mass flows over into the neighbouring valley. In a phase with a continuous flow of mass, the donor star will fill the maximum volume available to it, its Roche lobe. The mass flows to the less extended accretor, which resides well inside its own lobe. The binary is said to be **semi-detached**.

Roche-lobe overflow starts either when one of the stars attempts to grow beyond its lobe, or because the lobe closes in on the star. The former can occur simply as a result of the star's nuclear evolution, e.g. when the star expands to become a giant. The latter can occur if the orbit shrinks by losing orbital angular momentum. We shall come back to both possibilities in Chapter 2.

There is yet another way to establish mass transfer, as indicated in the lower panel of Figure 1.10. Massive stars and giant stars display rather strong stellar winds (see also Chapter 7). The accretor can capture some fraction of the matter lost by the other star in its wind. Hence mass is transferred even though the mass-losing star is well inside its Roche lobe. This mode of mass transfer is called **wind accretion**. Most of the mass in the wind is lost from the binary, however.

Figure 1.11 depicts an artist's impression of a semi-detached binary with a white dwarf accretor, while Figure 1.12 presents a sketch of the black hole binaries known at the time of writing (2008), drawn to scale. The images show that matter leaving the donor star through the L_1 point settles into an accretion disc around the compact star. We now turn to accreting compact objects on much larger scales.

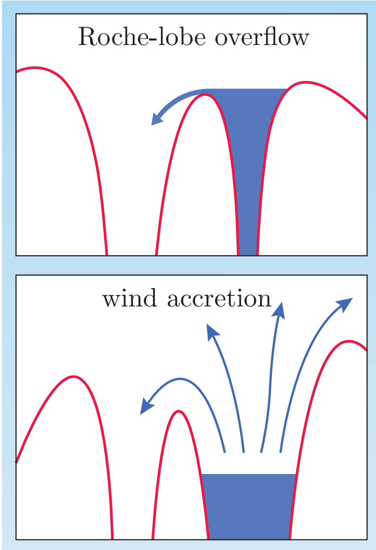

Figure 1.10 Schematic view of Roche-lobe overflow and wind accretion.

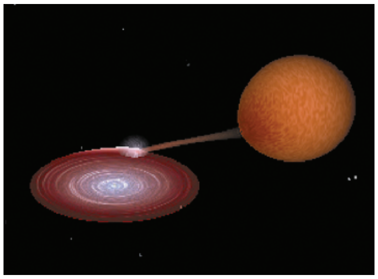

Figure 1.11 An artist's impression of a **cataclysmic variable star** — a compact binary where a white dwarf accretes from a Roche-lobe filling normal star.

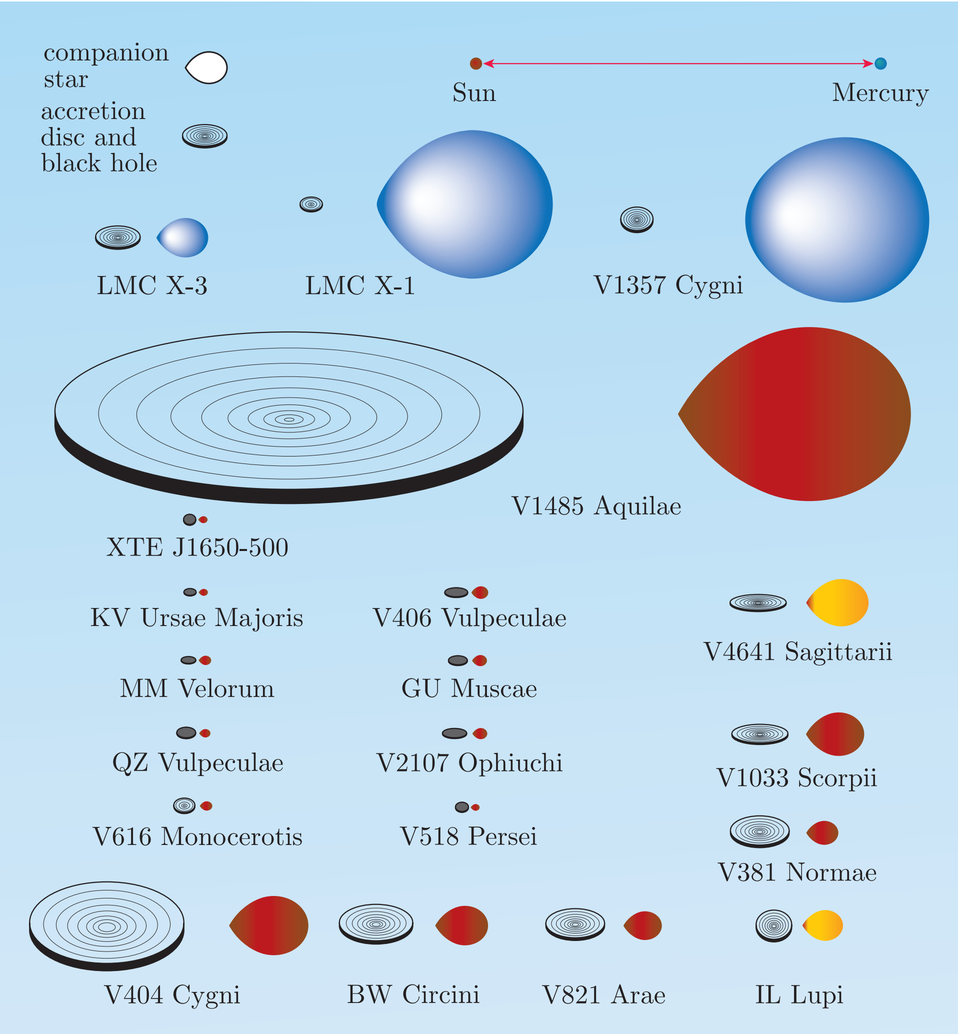

Figure 1.12 Known compact binaries with a black hole accretor, on a scale based on the distance between the Sun and Mercury, indicated at the top of the figure. The colour of the companion (donor) star indicates its surface temperature: dark red is cool, bright yellow is hot. (Courtesy of Jerry Orosz.)

1.3.2 Active galactic nuclei

An **active galaxy** contains a bright, compact nucleus that dominates its host galaxy's radiation output in most wavelength ranges. These **active galactic nuclei** (or **AGN**) are thought to be powered by a supermassive black hole (the engine) that accretes from a large hot accretion disc. The disc is the source of the continuum emission in the ultraviolet and X-ray bands, while an obscuring dust torus surrounding the disc emits in the infrared (Figure 1.13).

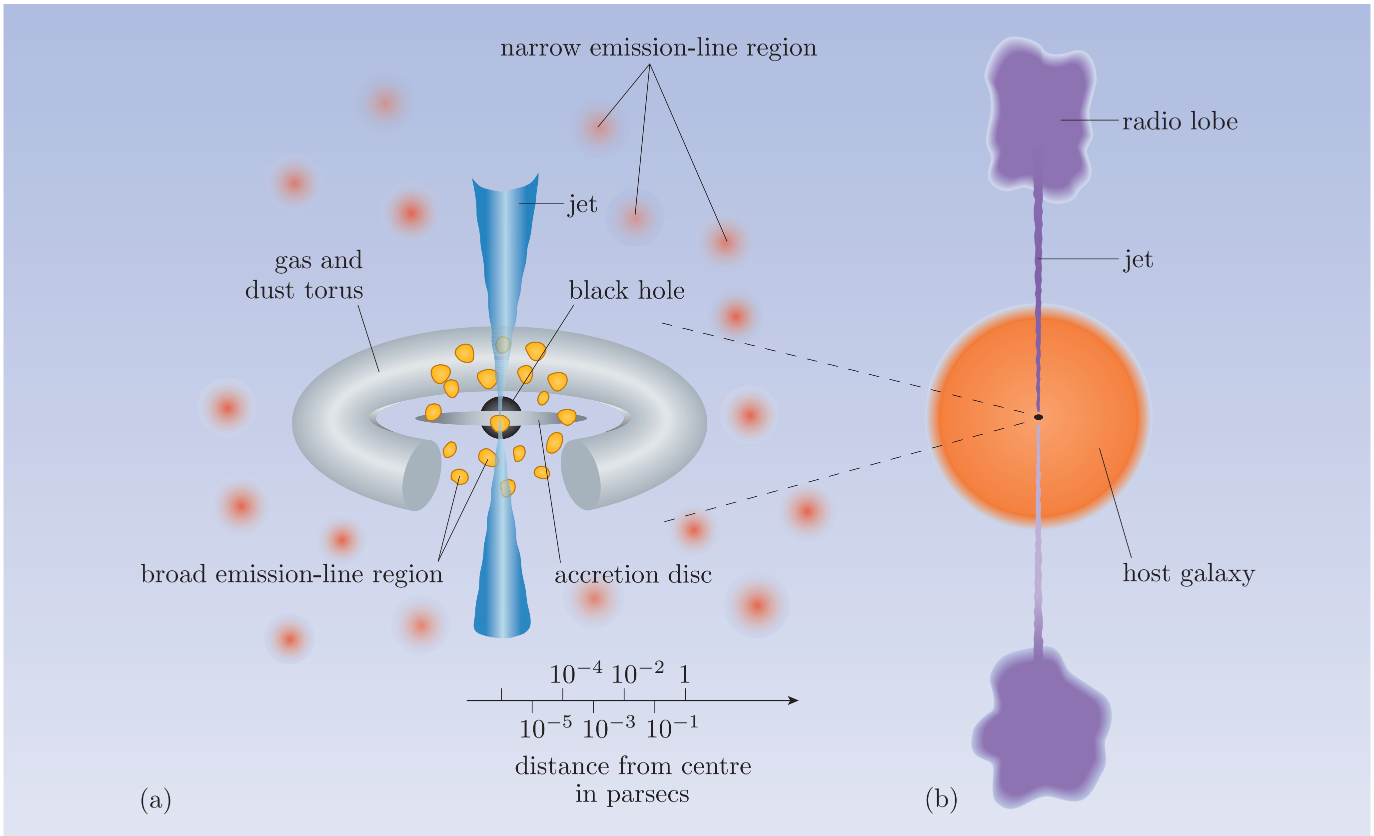

Figure 1.13 A generic model for an active galaxy. (a) A supermassive black hole is surrounded by an accretion disc; jets emerge perpendicular to it. An obscuring torus of gas and dust encloses the broad-line region (a few light-days across) with the narrow-line region (a few hundred parsecs across) lying further out. (b) The entire AGN appears as a bright nucleus in an otherwise normal galaxy, while jets (hundreds of kiloparsecs in length) terminate in radio lobes.

Active galaxies come in many disguises, and consequently they can be grouped in numerous classes with quite diverse observed properties. Unified models attempt to explain this range of AGN on the assumption that they differ only in luminosity and the angle at which they are viewed.

One broad classification criterion is based on the observed activity in the radio band; there are weak and strong radio emitters. The most important representatives of AGN that display no or only a very weak radio emission are **Seyfert galaxies** and **quasars** (although $\lesssim 10\%$ of quasars are strong radio sources; it is these that created the name quasars — *quasi-stellar radio sources*).

Seyfert galaxies look like normal galaxies, but with an unusual luminous nucleus. The host galaxies of quasars are so distant and so much fainter than the point-like (quasi-stellar) nucleus that they are seen only on deep images taken with the most powerful telescopes. The point-like nucleus, on the other hand, can be easily detected.

Among the strong radio-emitting active galaxies are **radio galaxies** and **blazars** which, like quasars, appear star-like. Many radio-bright active galaxies display prominent, narrowly focused jets that emanate from the AGN in opposite directions and often extend to distances exceeding the size of the host galaxy.

The active nucleus of Seyfert galaxies easily outshines its entire host galaxy, demonstrating that the intrinsic AGN luminosity must be very large indeed. Values in the range 10^{11}–$10^{15}\,\mathrm{L}_\odot$ are commonly derived from the observed flux and the large distances implied by the observed cosmological redshift of AGN emission lines. The evidence for the existence of an accreting supermassive black hole that could generate the enormous emitting power of AGN is circumstantial but very compelling. The AGN central engine must fit in a very small volume of space, and this small volume must contain a very large amount of gravitating mass. We now look at both of these facts in detail.

Compactness

Not only do the active nuclei of even the closest Seyfert galaxies appear as unresolved point sources of light, but the luminosities of some AGN are also seen to vary significantly over a few days. This means that the time Δt for light to travel across the entire source must be only a few days, because otherwise the changes in luminosity would be smoothed out by the delayed arrival times of the photons from the more distant regions of the source. This can be expressed by the general requirement that

$$l \lesssim \Delta t \times c,$$

where l is the size of the emitting source and Δt is the timescale for observed variability. Using this to work out the size limit corresponding to a **light travel time** of a few days, we have

$$l \lesssim 10 \times 24 \times 60 \times 60 \times 3 \times 10^8\,\mathrm{m},$$

where we have adopted a typical value of $\Delta t = 10$ days, converted this into seconds, and used an approximate value for the speed of light: $c \approx 3 \times 10^8\,\mathrm{m\,s^{-1}}$. Evaluating, and retaining only 1 significant figure, we have

$$l \lesssim 3 \times 10^{14}\,\mathrm{m},$$

which can be converted into length units more convenient for astronomical objects:

$$l \lesssim \frac{3 \times 10^{14}\,\mathrm{m}}{1.5 \times 10^{11}\,\mathrm{m\,AU^{-1}}}, \quad \text{i.e.} \quad l \lesssim 2 \times 10^3\,\mathrm{AU}. \tag{1.17}$$

Thus the observations require that a luminosity of perhaps a 100 times that of the entire Milky Way galaxy be generated within a region with diameter only about 1000 times that of the Earth's orbit!

Exercise 1.7 Convert the length scale in Equation 1.17 into parsecs (pc). ■

Mass

The second piece of evidence for the existence of a supermassive black hole as the engine of AGN is based on the **virial theorem** (see the box on page 14). In the AGN context this can be recast in terms of the mean (or typical) velocity of a large number of individual bodies that are all part of the gravitating system. If the total mass of the gravitating system is M and its radial extent is r, then Equation 1.6 can be written as

$$\frac{1}{2}m\langle v^2\rangle \simeq \frac{1}{2}\frac{GMm}{r}, \tag{1.18}$$

where m is a typical mass of these bodies, and $\langle v^2\rangle$ is the mean value of the squares of their speeds with respect to the centre of mass. Hence

$$\langle v^2\rangle \simeq \frac{GM}{r}. \tag{1.19}$$

The motion of these bodies — stars and clouds or blobs of gas — will give rise to **Doppler broadening** of the spectral lines that they emit. As the AGN emitting region is so small, the observer will only see the superposition of the emission lines from individual emitters, all Doppler-shifted by their corresponding radial velocity. The combined emission line will therefore have a line profile width that reflects the average velocity $\langle v\rangle$ of the individual emitters. This is also called the **velocity dispersion**.

The velocity dispersion measured for the so-called broad-line region of AGN, which is contained within the torus of infrared emitting dust (see Figure 1.13), is typically observed to be 10^3–$10^4\,\mathrm{km\,s^{-1}}$. The observed variability of the line-emitting region implies that it is a few tens of light-days across. (We shall discuss the broad-line region in more detail in Section 5.4 below.) Hence the virial theorem gives the mass of the central black hole as approximately 10^7–$10^{11}\,\mathrm{M_\odot}$. The label *supermassive* seems to be well justified.

Exercise 1.8 Confirm the above statements by calculating the mass of the central black hole if the emitting region is ≈ 30 light-days across, and displays Doppler broadening of $6000\,\mathrm{km\,s^{-1}}$. ■

Supermassive black holes in galactic nuclei

It is now thought that most galaxies harbour a supermassive black hole (with mass $\gtrsim 10^6\,\mathrm{M_\odot}$) in the centre. In active galaxies this black hole is accreting and a strong power source, while in normal galaxies such as the Milky Way the black hole lies dormant. The crucial evidence comes from the observation of the motion of stars near the centre of the galaxy.

Perhaps the most dramatic example is the case of the supermassive black hole at the centre of our own Milky Way galaxy. This region is impossible to study in optical light because there is a lot of gas and dust in the plane of the galaxy, which obscures our view of the central regions. At other wavelengths, however, the optical depth is less, and it has long been known that the centre of our galaxy harbours a compact radio source, which is called Sgr A* and is shown in Figure 1.14. Apart from Sgr A*, the radio emission apparent from Figure 1.14 is diffuse and filamentary. The stars near the centre of the Galaxy are not visible because they are not strong radio sources. The infrared view shown in the left

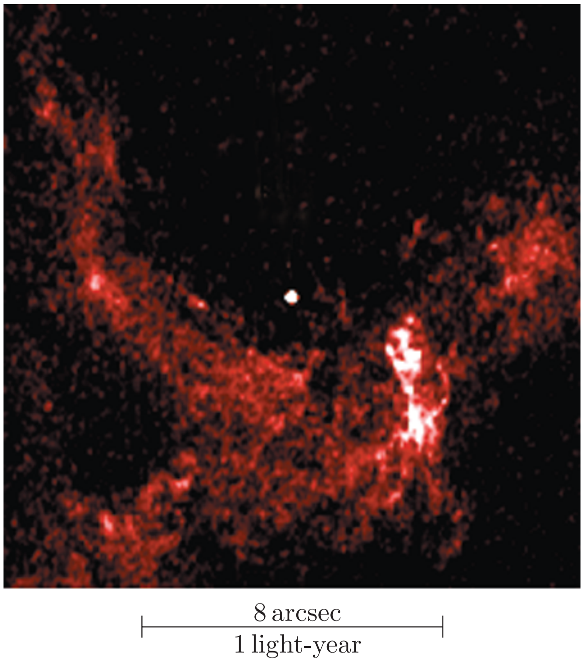

Figure 1.14 A radio image of the centre of the Milky Way. White areas indicate intense radio emission, and the red and black areas are progressively less intense. This image was taken with the Very Large Array (VLA) by Jun-Hui Zhao and W. M. Goss. The white dot at the centre of the image is the Sgr A* compact radio source.

panel of Figure 1.15 is very different. The image is **diffraction-limited**, and gives a resolution of 0.060 arcseconds. The blobs are individual stars within 60 light-days of the Sgr A* radio source, whose position is marked with the small cross at the centre of Figure 1.15.

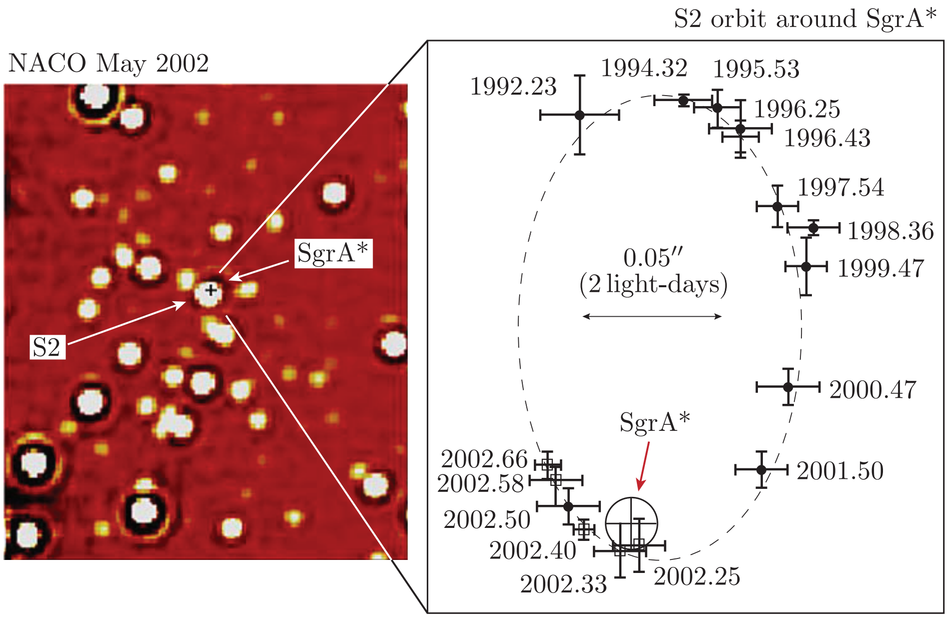

Figure 1.15 (a) An infrared image from May 2002 at 2.1 μm wavelength of the region near Sgr A* (marked by the cross). The image is about 1.3 arcseconds wide, corresponding to about 60 light-days. (b) The orbit of S2 as observed between 1992 and 2002, relative to Sgr A* (marked with a circle). The positions of S2 at the different epochs are indicated by crosses, with the dates (expressed in fractions of the year) shown at each point. The solid curve is the best-fitting elliptical orbit — one of the foci is at the position of Sgr A*.

- How do the scales of the images in Figure 1.14 and Figure 1.15 (left panel) compare?
- The bar in Figure 1.14 represents 8 arcseconds, while the image in Figure 1.15 is less than 2 arcseconds across.

The left panel of Figure 1.15 is only one frame of a series of high spatial resolution infrared images of the centre of our galaxy, which were taken starting in the early 1990s. The motions of individual stars are clearly apparent when subsequent frames are compared. The right panel of Figure1.15 shows the example of the star S2, which can be clearly seen to orbit Sgr A* with a period of about 15 years! A number of such stellar orbits have now been measured, and from Kepler's law the gravitating mass inside the orbit can be determined. This is analogous to the determination of the Sun's gravitational field (and hence the Sun's mass) by studying the orbits of the planets in the solar system. The stars at the centre of the Galaxy are not neatly aligned in a plane analogous to the ecliptic in the solar system. Instead, the stars follow randomly oriented orbits. The observed motions require the presence of a dark body with mass $4 \times 10^6\,\mathrm{M}_\odot$ at the centre of our galaxy. This dark central body is almost certainly a black hole.

In galaxies where the orbits of stars or clouds cannot be mapped in this detail, the virial theorem is used to deduce the gravitational field from the observed dispersion of the velocity of the detected individual moving sources.

1.4 Radiation from accretion flows

As accretion flows often take the form of a disc-like structure, we now investigate the basic appearance of such accretion discs, as indicated by the temperature of the disc. We shall return to the physics of accretion discs in greater detail in Chapters 3 and 4.

1.4.1 Temperature of an accreting plasma

We wish to arrive at a quantitative estimate for the temperature of the accretion disc plasma as it approaches the accretor. To this end we make two assumptions. First, all of the locally liberated gravitational potential energy is instantly converted into thermal energy. Second, photons undergo many interactions with the local stellar plasma and are thermalized before they emerge from the surface of the disc. In other words, the plasma is **optically thick** and radiates locally like a black body.

As we shall see in Subsection 3.4.4, the accretion disc surface temperature T_{eff} of a geometrically thin, optically thick steady-state accretion disc varies with distance r from the accretor as

$$T_{\text{eff}}^4(r) \simeq \frac{3GM\dot{M}}{8\pi\sigma r^3}. \qquad (1.20)$$

This relation holds if r is large compared to the inner disc radius. The exact form of the profile peaks very close to the inner disc radius R, at a temperature

$$T_{\text{peak}} \simeq 0.5 \times \left(\frac{3GM\dot{M}}{8\pi\sigma R^3}\right)^{1/4}. \qquad (1.21)$$

In a steady-state disc, the local mass accretion rate at each radius r is the same in each disc annulus, and in fact equals the mass accretion rate $\dot{M}$ onto the central object.

It is easy to see that a relation of the form $T_{\text{eff}}^4 \propto GM\dot{M}/r^3$ must apply. Consider a disc annulus at radius r and width Δr (hence area $\propto r\Delta r$). The gravitational potential energy (Equation 1.1) changes across the annulus per unit time by

$$\frac{\mathrm{d}E_{\text{GR}}}{\mathrm{d}r} \propto \frac{\mathrm{d}(GM\dot{M}/r)}{\mathrm{d}r} \propto \frac{GM\dot{M}}{r^2}.$$

The energy dissipated per unit area in the annulus is therefore $\propto GM\dot{M}/r^3$. By assumption, the liberated energy heats up the disc annulus to a temperature T_{eff}, which in turn radiates as a black body through thermal emission. The flux F emitted by a black body source, i.e. the energy emitted per unit time per unit area, is given by the Stefan–Boltzmann law

$$F = \sigma T_{\text{eff}}^4, \qquad (1.22)$$

where σ is the Stefan–Boltzmann constant. Now F must equal the rate of energy generation, so $F \propto T_{\text{eff}}^4 \propto GM\dot{M}/r^3$. (A more detailed derivation is presented in Chapter 3.)

Equation 1.20 states that accreting plasma heats up with decreasing distance from the centre as $T_{\text{eff}} \propto r^{-3/4}$, so material will become very hot as it approaches a compact object. Temperatures in excess of 10^5 K in the case of white dwarfs and 10^7 K for neutron stars are the norm.

Exercise 1.9 Calculate the peak temperature of an accretion disc:
(a) around a white dwarf with mass $0.6\,\mathrm{M}_\odot$ and radius $R = 8.7 \times 10^6$ m for an accretion rate of $10^{-9}\,\mathrm{M}_\odot\,\mathrm{yr}^{-1}$ (which is typically observed in cataclysmic variables with a few hours orbital period);
(b) around a neutron star with mass $1.4\,\mathrm{M}_\odot$ and radius $R = 10$ km for an accretion rate of $10^{-8}\,\mathrm{M}_\odot\,\mathrm{yr}^{-1}$ (observed in some bright neutron star X-ray binaries).

Exercise 1.10 (a) Express the peak temperature of an accretion disc around a Schwarzschild black hole in terms of the mass accretion rate in units of $\mathrm{M}_\odot\,\mathrm{yr}^{-1}$ and the black hole mass in units of $\mathrm{M}_\odot$. Assume that the inner edge of the accretion disc is at a radius $3R_{\mathrm{S}}$.

(b) Calculate the peak disc temperature for a black hole with mass $10\,\mathrm{M}_\odot$ and accretion rate $10^{-7}\,\mathrm{M}_\odot\,\mathrm{yr}^{-1}$, as in bright low-mass X-ray binaries.

(c) Calculate the peak disc temperature for a black hole with mass $10^7\,\mathrm{M}_\odot$ and accretion rate $1\,\mathrm{M}_\odot\,\mathrm{yr}^{-1}$, as in AGN. ■

1.4.2 Continuum emission

Stellar matter at such high temperatures emits electromagnetic waves of very high frequencies, so compact binaries are powerful sources of high-energy radiation.

The brightest sources in the X-ray sky are in fact accreting neutron star and black hole binaries (see Figure 1.16). Several hundreds of these **X-ray binaries** reside in the Milky Way, and many more are known in distant, external galaxies.

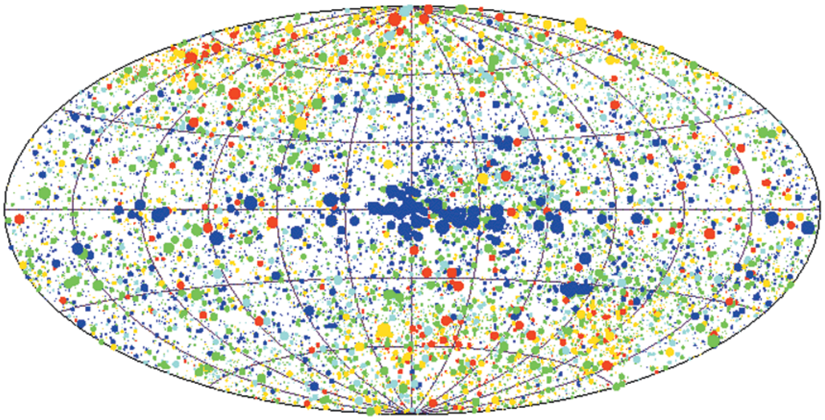

Figure 1.16 An all-sky map of the X-ray sky as seen by the X-ray satellite ROSAT. The colour of the dots indicates the 'X-ray colour', i.e. the spectral characteristics of the X-ray source. The size of the dots indicates the intensity of the emitted X-rays. The celestial sphere has been mapped into the plane of the page such that the Galactic Equator (the band of the Milky Way on the sky) appears as the horizontal line in the middle of the diagram. Along the Galactic Equator the Galactic longitude changes from $-180°$ at the left to $+180°$ at the right. The Galactic Centre is in the middle. The vertical line in the middle joins the Galactic North Pole (top) with the Galactic South Pole (bottom).

The mass M_2 of the compact object's companion star can be used to separate X-ray binaries into two main groups with distinct properties, which we shall discuss in Chapters 2 and 6. In **low-mass X-ray binaries**, or **LMXBs** (Figure 1.17), the companion star is a low-mass star ($M_2 \lesssim 2\,\mathrm{M}_\odot$), while in **high-mass X-ray binaries**, or **HMXBs** (Figure 1.18), this is a massive star ($M_2 \gtrsim 10\,\mathrm{M}_\odot$). Companion stars with masses in between these limits are much less commonly observed but theoretically implied, and are sometimes referred to as **intermediate-mass X-ray binaries**.

The discs in AGN are much larger than in X-ray binaries, but they are not quite as hot (see Exercise 1.10). The observed AGN X-ray emission is likely to be reprocessed thermal emission from the underlying accretion discs. This will be discussed further in Chapter 6 (Subsection 6.3.2 and Section 6.7). AGN still emit about 10% of their total energy budget in the X-ray band, and the fact that the emission is highly variable demonstrates that it is generated in the innermost regions near the compact object. Therefore AGN are much more powerful X-ray emitters than X-ray binaries, but the nearest AGN is so far away that the X-ray flux we receive from it is smaller than the received flux from bright X-ray binaries in the Galaxy. Yet AGN are ubiquitous across the X-ray sky and are the dominant X-ray source group for faint X-ray fluxes. In nearby galaxies it is often difficult to tell if an X-ray source is an X-ray binary residing in this galaxy, or an unrelated, distant AGN that happens to be in the same line of sight as the nearby galaxy.

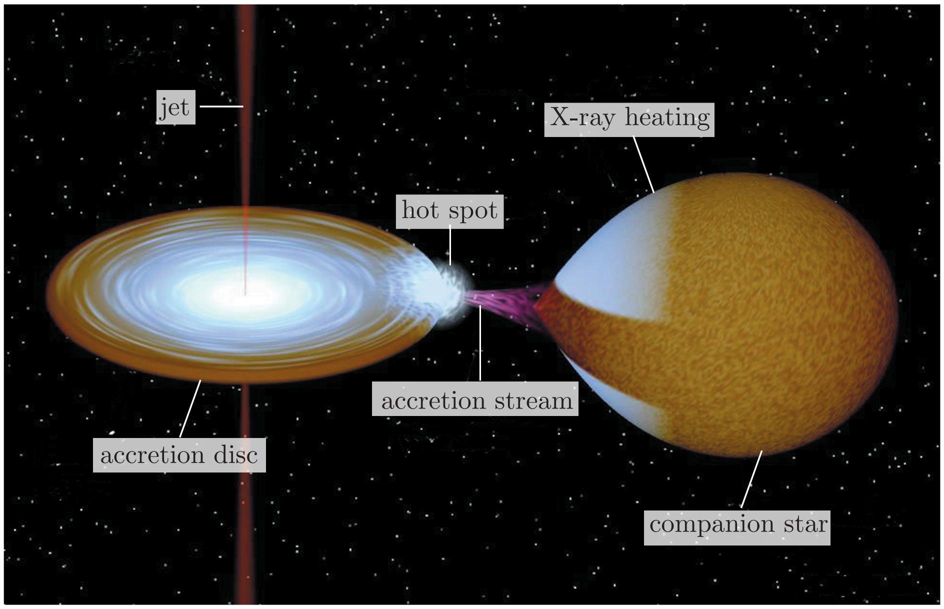

Figure 1.17 Artist's impressions of the low-mass X-ray binary V1033 Scorpii (also known as GRO J1655-40), which is a superluminal jet source (see also Chapter 7). The black hole accretes matter from a Roche-lobe filling low-mass or intermediate-mass companion star. The orbital period is 2.6 days. (Courtesy of Rob Hynes.)

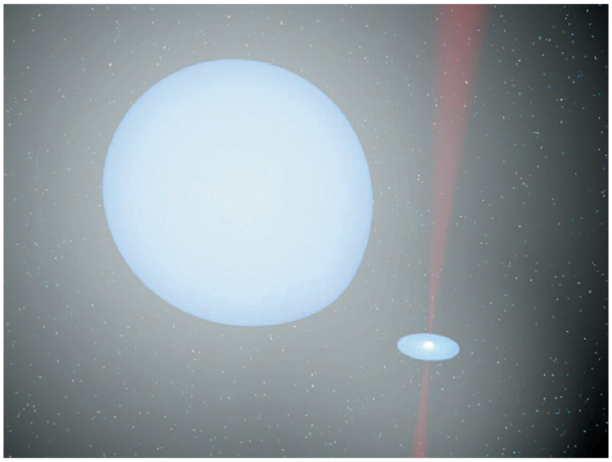

Figure 1.18 Artist's impression of the high-mass X-ray binary Cygnus X-1. The black hole accretes from the wind of the massive companion star. The orbital period is 5.6 days. (Courtesy of Rob Hynes.)

To better understand the continuum emission of accretion discs with compact accretors, we now recall the properties of black body radiation. In the idealized case considered above, each disc annulus radiates as a black body with the surface temperature T_{eff} of the annulus.

Black body radiation

Black body radiation is in thermal equilibrium with matter at a fixed temperature. Often the emission from astronomical objects is a close approximation to this **thermal radiation**. Many thermal sources of radiation, for instance stars, have spectra which resemble the black body spectrum, which is described by the Planck function

$$B_\nu(T) = \left(\frac{2h\nu^3}{c^2}\right)\frac{1}{\exp(h\nu/kT) - 1}. \tag{1.23}$$

The quantity B_ν is the power emitted by per unit area per unit frequency per unit solid angle (and has the units $\mathrm{W\,m^{-2}\,Hz^{-1}\,sr^{-1}}$); k is the Boltzmann constant, and h is Planck's constant.

Figure 1.19 illustrates the way that black body spectra peak at wavelengths that depend on temperature. This is quantified by the **Wien displacement law**, which states that the maximum value of B_ν shown in Figure 1.19 occurs at a wavelength λ_{max} determined by

$$\lambda_{\text{max}} T = 5.1 \times 10^{-3}\,\text{m K}. \tag{1.24}$$

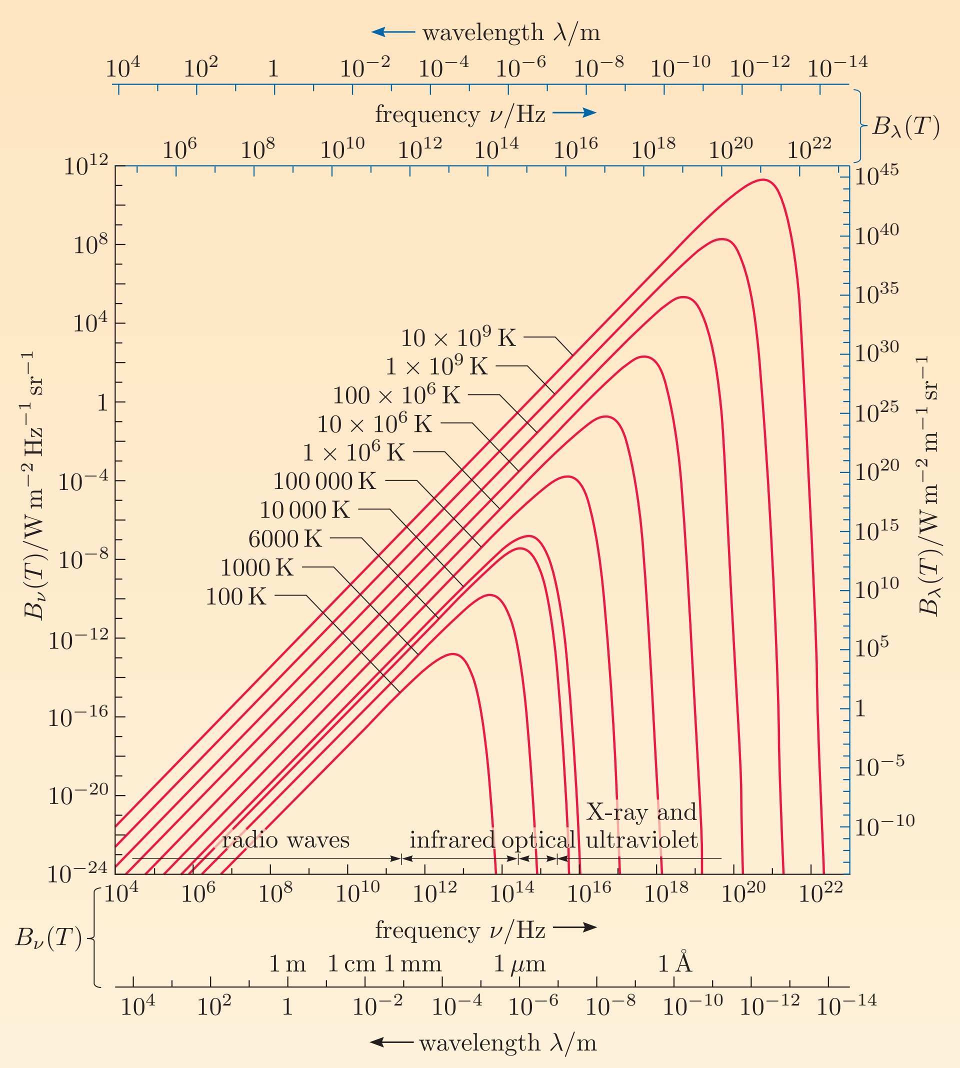

Figure 1.19 The black body spectrum for various temperatures. The peak emission occurs at a wavelength described by the Wien displacement law. The shape at substantially longer wavelengths is known as the Rayleigh–Jeans tail; at substantially shorter wavelengths it is the Wien tail.

The figure also shows that the emitted power of a black body increases at all wavelengths as the temperature increases. So a hotter black body will be brighter than a cooler black body even at the peak wavelength of the latter.

A useful way of characterizing the black body emission is in terms of its mean photon energy

$$\langle E_{\text{ph}} \rangle = 2.70kT. \tag{1.25}$$

The typical thermal energy of particles in a gas with temperature T is the same as the mean photon energy $\langle E_{\rm ph} \rangle$.

Photon temperature

Photon energies are often expressed in electronvolts rather than joules, where $1\,\mathrm{eV} = 1.602 \times 10^{-19}$ J. In the context of the high-energy emission of astrophysical bodies, it is common practice to quote the photon energy as a temperature, $T \simeq E_{\rm ph}/k$, obtained by inverting Equation 1.25. This concept of a radiation temperature is enormously useful when attempting to estimate the radiation expected from a gas or plasma with a certain temperature. The rule of thumb

$$1\,\mathrm{eV} \text{ corresponds to } 10^4\,\mathrm{K} \tag{1.26}$$

is worth remembering.

Exercise 1.11 Verify Equation 1.26.

Exercise 1.12 (a) Calculate the typical photon energies for the accretion discs considered in Exercises 1.9 and 1.10. Express the results in eV.

(b) Calculate the corresponding wavelengths, and compare them to the wavelength range of visible light. ■

The shape of the Planck function at substantially shorter wavelengths than the peak (high energies) is known as the **Wien tail**, which is described by

$$B_\nu(T) = (2h\nu^3/c^2)\exp(-h\nu/kT). \tag{1.27}$$

The shape of the Planck function at substantially longer wavelengths than the peak (low energies) is known as the **Rayleigh–Jeans tail**, which is described by

$$B_\nu(T) = 2kT\nu^2/c^2. \tag{1.28}$$

These ‘tails’ at both extremes of wavelength are sometimes referred to as the long-wavelength (or low-energy) cut-off and the short-wavelength (or high-energy) cut-off.

Exercise 1.13 Show that the Planck function (Equation 1.23) depicted in Figure 1.19 adopts the functional form expressed in Equation 1.27 for large frequencies, and the functional form expressed in Equation 1.28 for small frequencies. ■

Multi-colour black body spectrum

Accretion discs can be thought of as composed of a series of annuli with different radii r, all emitting locally as a black body (Equation 1.23) with temperature $T(r) = T_{\rm eff}(r)$ as calculated in Equation 1.20. The resulting continuum emission spectrum is a sum of black body spectra at different T, but the dominant contribution will come from the region where the accreting plasma is hottest, i.e. from the vicinity of the inner edge of the disc. We consider this now in detail.

The total output from the disc is obtained by summing the contributions of all disc annuli, i.e. by the integral

$$F_\nu \propto \frac{1}{D^2}\int_{r_{\rm in}}^{r_{\rm out}} \left(\frac{2h\nu^3}{c^2}\right)\frac{1}{\exp(h\nu/kT_{\rm eff}(r))-1}\,2\pi r\,{\rm d}r \tag{1.29}$$

from the inner disc radius $r_{\rm in}$ to the outer disc radius $r_{\rm out}$. The flux F_ν per unit frequency received by the observer scales as $1/D^2$, where D is the distance between observer and emitter. The azimuthal part of the integral in Equation 1.29 has already been carried out and gave the factor 2π.

We have $T_{\rm eff}^4 \propto r^{-3}$, so the hottest black body that contributes has approximately the temperature $T_{\rm eff}(r_{\rm in}) \equiv T_{\rm in}$, while the coolest black body that contributes has the temperature $T_{\rm eff}(r_{\rm out}) \equiv T_{\rm out}$.

We consider now the shape of the disc spectrum F_ν in three different regimes.

For $h\nu \ll kT_{\rm out}$, i.e. for low-energy photons, cooler than the coolest part of the disc, the Planck function adopts the form of the Rayleigh–Jeans tail (Equation 1.28), and the integral can be written as

$$F_\nu \propto \int \nu^2 T_{\rm eff}(r) r\,{\rm d}r \propto \nu^2 \int T_{\rm eff}(r) r\,{\rm d}r, \tag{1.30}$$

i.e. the disc spectrum at low frequencies also has the characteristic Rayleigh–Jeans tail shape, $F_\nu \propto \nu^2$, as the integral in Equation 1.30 is independent of ν.

For $h\nu \gg kT_{\rm in}$, i.e. for high-energy photons, hotter than the hottest part of the disc, the Planck functions adopts the form of the Wien tail (Equation 1.27), and the integral can be written as

$$F_\nu \propto \nu^3 \int \exp(-h\nu/kT_{\rm eff}(r)) r\,{\rm d}r. \tag{1.31}$$

The integral is proportional to the difference in the values of $\exp(-h\nu/kT_{\rm eff}(r))$ at the inner and outer disc radii. As $h\nu/kT_{\rm out}$ is much larger than $h\nu/kT_{\rm in}$, the term with $T_{\rm out}$ is negligible. So the integral scales as $\exp(-h\nu/kT_{\rm in})$, and we have

$$F_\nu \propto \nu^3 \exp(-h\nu/kT_{\rm in}), \tag{1.32}$$

i.e. the disc spectrum has a Wien tail that corresponds to the temperature of the innermost disc.

For the intermediate range of photon energies, much larger than the thermal energies at the outer disc but much smaller than those at the inner disc, i.e. for $kT_{\rm out} \ll h\nu \ll kT_{\rm in}$, we define

$$x = \frac{h\nu}{kT_{\rm eff}(r)} = \varepsilon\nu r^{3/4}, \tag{1.33}$$

$\varepsilon = (h/k)(8\pi\sigma/3GM\dot{M})^{1/4}$ can be obtained from Equation 1.20 when $T_{\rm eff}$ is expressed in terms of r.

where ε is a constant for a system with a given mass and mass accretion rate. We therefore have $r = (x/\varepsilon\nu)^{4/3}$ and

$$\frac{{\rm d}r}{{\rm d}x} = \frac{4}{3}\frac{x^{1/3}}{(\varepsilon\nu)^{4/3}}. \tag{1.34}$$

Expressing Equation 1.29 in terms of x, we obtain

$$\begin{aligned} F_\nu &\propto \int_{x_{\rm in}}^{x_{\rm out}} \nu^3 \frac{1}{e^x-1} \times \left(\frac{x}{\nu}\right)^{4/3} \times \frac{x^{1/3}}{\nu^{4/3}}\,{\rm d}x \\ &\propto \nu^{1/3}\int_{x_{\rm in}}^{x_{\rm out}} \frac{x^{5/3}}{e^x-1}\,{\rm d}x. \end{aligned}$$

As $x_{\text{in}} \ll 1$ and $x_{\text{out}} \gg 1$, the integral is approximately equal to

$$\int_0^\infty \frac{x^{5/3}}{e^x - 1}\,\mathrm{d}x,$$

and is therefore independent of ν. So we have

$$F_\nu \propto \nu^{1/3}, \tag{1.35}$$

which is a spectral shape that is often quoted as characteristic for an accretion disc. The width of the frequency range over which the disc spectrum does indeed follow the $\nu^{1/3}$ relation depends on the difference between the inner and outer disc temperatures; see Figure 1.20.

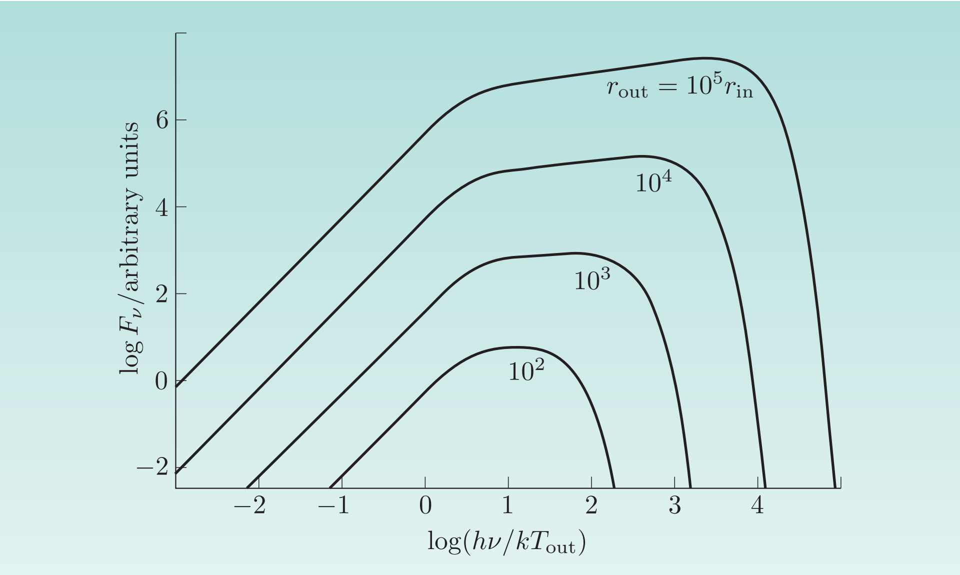

Figure 1.20 The spectrum of an accretion disc that emits locally like a black body, for different ratios of outer to inner disc radius.

Summary of Chapter 1

1. The process where a gravitating body grows in mass by accumulating matter from an external reservoir is called mass accretion. The accretion luminosity of a body with mass M and radius R is

$$L_{\text{acc}} = \frac{GM\dot{M}}{R}, \tag{Eqn 1.3}$$

where $\dot{M}$ is the accretion rate. A useful unit for the accretion rate is

$$1\,\mathrm{M_\odot\,yr^{-1}} = 6.31 \times 10^{22}\,\mathrm{kg\,s^{-1}}. \tag{Eqn 1.4}$$

2. The conservation of angular momentum implies that the accreting material will in general settle into an accretion disc around the accretor. The orbital motion of disc material can be approximated well by Kepler orbits, with a slow, superimposed radial drift towards the accretor. As the accreting plasma slowly drifts inwards, gravitational potential energy is lost. Half of this energy is converted into kinetic energy, while the other half is available to heat the plasma and to power the emission of electromagnetic radiation.

3. The accretion efficiency η_{acc}, defined by

$$L_{\text{acc}} = \eta_{\text{acc}} \dot{M} c^2, \qquad \text{(Eqn 1.9)}$$

expresses the rate of energy gained by the accretion of matter, in units of the mass energy of that matter. Accretion onto compact objects (white dwarfs, neutron stars and black holes) returns a very large accretion efficiency, much larger than the efficiency for hydrogen burning, the energy source powering main-sequence stars.

4. A non-rotating (Schwarzschild) black hole is formed when a mass M collapses to within a sphere of radius R_{S}, where

$$R_{\text{S}} = \frac{2GM}{c^2}. \qquad \text{(Eqn 1.11)}$$

The Schwarzschild radius R_{S} is the radius of the sphere surrounding the collapsed mass at which the escape speed equals the speed of light. The general relativistic result for the accretion efficiency of a disc-accreting Schwarzschild black hole is $\eta_{\text{acc}} = 5.7\%$. For a Kerr black hole with maximum pro-grade spin this efficiency is $\eta_{\text{acc}} = 32\%$.

5. Both Schwarzschild and Kerr black holes represent gravitational singularities where the curvature of spacetime is infinite. In the case of Kerr black holes this singularity is a ring in the plane perpendicular to the rotational axis, while it is a single point for Schwarzschild black holes. Both types have a spherical event horizon where the escape speed is the speed of light. A Kerr black hole is surrounded by a second, larger critical surface, the static limit, which has the shape of an oblate spheroid and touches the event horizon at its poles. The space between these two surfaces is called the ergosphere.

6. A binary star is a system consisting of two stars that orbit the common centre of mass. A compact binary is a close binary system where one component is a compact star. If the orbital separation is of order the stellar radii, the binary components can interact by exchanging mass.

7. Mass transfer in binaries is best described in a frame of reference that co-rotates with the binary orbital motion. In such a frame there are two types of pseudo-forces: the centrifugal force of magnitude

$$F_{\text{c}} = m\frac{v^2}{r} = m\omega^2 r, \qquad \text{(Eqn 1.14)}$$

and the Coriolis force

$$\boldsymbol{F}_{\text{Coriolis}} = -2m\boldsymbol{\omega} \times \boldsymbol{v}, \qquad \text{(Eqn 1.15)}$$

which vanishes for a test mass at rest in the co-rotating frame.

8. The force on a test mass m in the binary frame can be obtained as $\boldsymbol{F} = -m\boldsymbol{\nabla}\Phi_{\text{R}}$, where the Roche potential Φ_{R} is given by

$$\Phi_{\text{R}}(\boldsymbol{r}) = -\frac{GM_1}{|\boldsymbol{r}-\boldsymbol{r}_1|} - \frac{GM_2}{|\boldsymbol{r}-\boldsymbol{r}_2|} - \tfrac{1}{2}\left(\boldsymbol{\omega} \times (\boldsymbol{r}-\boldsymbol{r}_{\text{c}})\right)^2. \qquad \text{(Eqn 1.16)}$$

The surface of a binary stellar component coincides with a Roche equipotential surface.

9. The inner Lagrangian point (L_1 point) is the point between the two stars where the force on a test mass vanishes. The L_1 point is a saddle point of the Roche potential. The Roche equipotential surface that contains L_1 consists of two closed surfaces that meet at L_1. The enclosed volume is the Roche lobe of the respective star. A stellar component of the binary can expand only until its surface coincides with this critical Roche equipotential. If such a Roche-lobe filling star attempts to expand further, mass will flow into the direction of smaller values of $\Phi_{\rm R}$, i.e. into the lobe of the second star. This is called Roche-lobe overflow. The binary is said to be semi-detached.
10. An active galaxy contains a bright, compact nucleus that dominates its host galaxy's radiation output in most wavelength ranges. These active galactic nuclei (or AGN) are thought to be powered by accretion onto supermassive black holes. AGN are very compact. From the timescale of AGN variability, the light-crossing time can be deduced to be only a few days.
11. The velocity dispersion in the broad-line region of AGN is typically observed to be several $10^3\,{\rm km\,s^{-1}}$, while the emitting region is seen to be smaller than a few tens of pc. Hence the virial theorem suggests that the mass of the central black hole is approximately 10^8–$10^{11}\,{\rm M_\odot}$.
12. Most galaxies harbour a supermassive black hole (with mass $\gtrsim 10^6\,{\rm M_\odot}$) in the centre. In active galaxies, this black hole is a strong power source, while in normal galaxies such as the Milky Way it lies dormant.
13. The radial temperature profile of an optically thick, steady-state accretion disc is approximately

$$T_{\rm eff}^4(r) \simeq \frac{3GM\dot{M}}{8\pi\sigma r^3}. \qquad \text{(Eqn 1.20)}$$

14. Accretion onto compact objects leads to very high plasma temperatures, 10^5–10^7 K. The corresponding black body emission peaks in the ultraviolet and X-ray regimes. The brightest sources in the X-ray sky are accreting neutron star and black hole binaries. In low-mass X-ray binaries, the companion star is a low-mass star ($M_2 \lesssim 2\,{\rm M_\odot}$), while in high-mass X-ray binaries, the companion star is a massive star ($M_2 \gtrsim 10\,{\rm M_\odot}$).
15. The thermal emission from an optically thick accretion disc is like a stretched-out black body. At high frequencies, the flux distribution F_ν has a Wien tail that corresponds to the temperature of the innermost disc. At low frequencies, the disc spectrum has the familiar Rayleigh–Jeans tail shape. The disc spectrum has a characteristic flat part $F_\nu \propto \nu^{1/3}$ at intermediate frequencies.

Acknowledgements

Grateful acknowledgement is made to the following sources:

Figures

Cover image: A multi-wavelength composite NASA image of the spiral galaxy M81, with X-ray data from the Chandra X-ray Observatory (blue), optical data from the Hubble Space Telescope (green), infrared data from the Spitzer Space Telescope (pink) and ultraviolet data from GALEX (purple). (Credit: X-ray: NASA/CXC/Wisconsin/D.Pooley & CfA/A.Zezas; Optical: NASA/ESA/CfA/A.Zezas; UV: NASA/JPL-Caltech/CfA/J.Huchra et al.; IR: NASA/JPL-Caltech/CfA). Superimposed is an artist's representation of M33 X-7, a black hole binary with a high-mass companion star. Credit: NASA/CXC/M.Weiss;

Figure 1.1: National Optical Astronomy Observatory; Figure 1.5: Source Unknown; Figure 1.9: adapted from Pringle, J. E. and Wade, R. A. (1985) 'Introduction', *Interacting Binary Stars*, Cambridge Astrophysics Series, CUP; Figure 1.11: Courtesy of Dan Rolfe, University of Leicester; Figure 1.12: Adapted from a figure created by Jerry Orosz, University of Utrecht; Figure 1.13: adapted from Ferrarese, L. Ford, H. (1996), *Space Science Reviews*, **116**, 523–624; Figure 1.14: Jun-Hui Zhao and W. M. Goss/AOC/NRAO; Figure 1.15: European Southern Observatory; Figures 1.17 and 1.18: Rob Hynes, University of Southampton; Figure 2.5: LISA International Science Team; Figure 2.8: Bulik, T. (2007) 'Black holes go extragalactic', *Nature*, **449**, 799, *Nature* Publishing Group; Figure 2.9: Bruce Balick (University of Washington), Vincent Icke (Leiden University, The Netherlands), Garrelt Mellema (Stockholm University), and NASA/ESA; Figure 2.10: courtesy of Bart Willems; Figure 2.11: adapted from Hobbs, G. et al. (2005) 'A statistical study of 233 pulsar proper motions', *Monthly Notices of The Royal Astronomical Society*, **360**, 974, Blackwell Science Limited; Figure 2.12: adapted from Danzmann K, Rüdiger A. (2003), *Class. Quantum Grav.* **20**, S1–S9; Figure 4.5: Constructed from observations made by the AAVSO, courtesy of John Cannizzo; Figures 5.1 and 5.4: Courtesy of Dan Rolfe, University of Leicester; Figure 5.2: adapted from Gilliland, R. L. et al. (1986) 'WZ Sagittae: time-resolved spectroscopy during quiescence', *Astrophysical Journal*, **301**, 252, The American Astrophysical Society; Figure 5.3: adapted from Horne, K. and Marsh, T. R. (1986) 'Emission line formation in accretion discs', *Monthly Notices of the Royal Astronomical Society*, **218**, 761, Blackwell Science Limited; Figure 5.5: adapted from Frank, J., King, A. and Raine, D. (2002) *Accretion Power in Astrophysics*, 3rd ed. CUP; Figure 5.6: adapted from Schoembs, R. et al. (1987) 'Simultaneous multicolour photometry of OY Carinae during quiescence', *Astronomy and Astrophysics*, **181**, 50, Springer–Verlag GmBH & Co; Figure 5.7: Courtesy of Raymundo Baptista, UFSC, Brazil; Figure 5.8: adapted from Tom Marsh, University of Southampton; Figure 5.9: adapted from Steeghs, D. (1999) Ph.D. thesis from University of St Andrews: 'Spiral waves in accretion discs', Danny Steeghs, University of Warwick; Figures 5.11 and 5.12: Danny Steeghs, University of Warwick; Figures 5.17: The Anglo–Australian Observatory/David Malin; Figure 6.1: Image courtesy of ESA; Figure 6.2: Josef Pöpsel; Figure 6.3: Barnard, R. Shaw-Greening, L. and Kolb, U. (2008) 'A multicoloured survey of NGC253 with XMM-Newton: testing the methods used for creating luminosity functions from low-count data', *Monthly*

Notices of the Royal Astronomical Society, **388**, 849, Blackwell Science Limited; Figure 6.5: D. de Chambure, XMM-Newton Project, ESA/ESTEC; Figure 6.8: adapted from Titarchuk, L, (1994) *Astrophysical Journal*, **434**, 570; Figure 6.9: adapted from Morrison, R. and McCammon, D. (1983) ‘Interstellar photoelectric absorption cross sections, 0.03-10 keV’, *Astrophysical Journal*, **270**, 119, The American Astronomical Society; Figure 6.15: adapted from Revnivtsev, M. et al. (2000) ‘High frequencies in the power spectrum of Cyg X-1 in the hard and soft spectral states’, *Astronomy and Astrophysics*, **363**, 1013, EDP Sciences; Figure 6.16: adapted from Strohmayer, T. and Bildsten, L. in Lewin, W. H. G. and van der Klis, M. (2006) Compact Stellar X-ray Sources, CUP; Figure 6.18: adapted from Boirin, L. et al. (2004) ‘Discovery of X-ray absorption lines from the low-mass X-ray binaries 4U 1916-053 and X 1254-690 with XMM Newton’, *Nuclear Physics*, Section B, **132**, 506, Elsevier Science; Figures 6.19 and 6.20: adapted from Church, M. J. and Balucinska-Church, M. (1995) ‘A complex continuum model for the low-mass X-ray binary dipping sources: application to X 1624-49’, *Astronomy and Astrophysics*, **300**, 441, EDP Sciences; Figure 6.23: Wijers, R. A. M. J. and Pringle, J. E. (1999) ‘Warped accretion discs and the long periods in X-ray binaries’, *Monthly Notices of the Royal Astronomical Society*, **308**, 207, Blackwell Publishers; Figure 6.25: adapted from van der Klis, M. et al. (1996) ‘Discovery of submillisecond quasi-periodic oscillations in the X-ray flux of Scorpius X-1’, *Astrophysical Journal*, **469**, 1, The American Astronomical Society; Figure 6.26: adapted from Done, C. and Gierlinski, M. (2003) ‘Observing the effects of the event horizon in black holes’, *Monthly Notices of the Royal Astronomical Society*, **342**, 1041, Blackwell Publishers; Figure 6.27: NASA Marshall Space Flight Center (NASA-MSFC); Figure 6.28: adapted from McHardy, I. (2006) ‘Long timescale X-ray variability of 3C273: similarity to Seyfert galaxies and Galactic binary systems’, Blazar Variability Workshop II: Entering the GLAST Era, ASP Conference Series, **350**, 94, Astronomical Society of the Pacific; Figure 6.29: adapted from Brenneman, L. W. and Reynolds, C. S. (2006) ‘Constraining black hole spin via X-ray spectroscopy’, *Astrophysical Journal*, **652**, 1028, The American Astronomical Society; Figures 7.1 and 7.2b: Images courtesy of NRAO/AUI; Figure 7.2a: Ann Wehrle and Steve Unwin/NASA; Figure 7.8: Marscher et al., Wolfgang Steffen, Cosmovision, NRAO/AUI/NSF; Figures 8.1 and 8.4: Courtesy of the Gamma-Ray Astronomy Team at the National Space Science and Technology Center (NSSTC), http://gammaray.nsstc.nasa.gov/batse/grb/; Figure 8.2 adapted from Schaeffer, B. et al. (1994), *The Astrophysical Journal Supplement Series*, **92**, 285, The American Astronomical Society; Figures 8.3a and 8.5: adapted from from Ph.D. thesis ‘Spectral studies of gamma-ray burst prompt emission’, by Y. Kaneko (2005) University of Alabama, Huntsville; Figure 8.3b: Fishman, G. J. (1999) ‘Observed properties of gamma-ray bursts’, *Astronomy and Astrophysics Supplement Series*, **138**, 395–398, The European Southern Observatory; Figure 8.6: adapted from Liang, E. W. et al. (2006) ‘Testing the curvature effect and internal origin of gamma-ray burst prompt emissions and X-ray flare with swift data’, *Astrophysical Journal*, **646**, 351, The American Astronomical Society; Figure 8.7: adapted from Stanek, K. Z. et al. (1999) ‘BVRI Observations of the optical afterglow of GRB 990510’, *Astrophysical Journal*, **522**, 39 The American Astronomical Society; Figure 8.8a: Taken from www.tls-tautenburg.de/research/klose/GRB030329.html; Figure 8.8b: Taken from http://www.mpe.mpg.de/∼jcg/grb030329.html; Figure 8.10: adapted from

Panaitescu, A. (2009) ‘Gamma-Ray Burst afterglows: theory and observations’, *American Institute of Physics Conference Proceedings*, **1133**, 127–138, American Institute of Physics; Figure 8.12: adapted from an original sketch by M. Ruffert and T. H. Janka; Figure 8.13: adapted from Zhang, W., Woosley, S. E. and MacFadyen, A. I. (2003) ‘Relativistic jets in collapsars’, *Astrophysical Journal*, **586**, 356, American Astronomical Society; Figure 8.14a: adapted from the original produced by Edo Berger (Harvard-Smithsonian CfA).

Every effort has been made to contact copyright holders. If any have been inadvertently overlooked the publishers will be pleased to make the necessary arrangements at the first opportunity.